International Journal of Thermal Sciences 160 (2021) 106695

Contents lists available at ScienceDirect

International Journal of Thermal Sciences

journal homepage: www.elsevier.com/locate/ijts

Complexity matters: Highly-accurate numerical models of coupled radiative–conductive heat transfer in a laser flash experiment

Artem Lunev [a,*], Vadim Zborovskii [b], Teymur Aliev [b]

[a] United Kingdom Atomic Energy Authority (UKAEA), Culham Science Centre, Abingdon, Oxfordshire OX14 3DB, United Kingdom
[b] P.N. Lebedev Physical Institute, Russian Academy of Sciences, Leninsky Prospect 53, Moscow 119991, Russia

ARTICLE INFO

Keywords:
Radiative transfer
Heat conduction
Discrete ordinates method
Thermal diffusivity

ABSTRACT

Opaque and fully dense solids respond to a laser pulse by absorbing its energy, causing non-uniform heating and thus creating a thermal gradient. Thermalisation by thermal conduction acts to minimise that gradient; monitoring this process as a function of time enables to infer the material properties such as thermal diffusivity. For samples with transparency in the near-infrared region (semi-transparent samples), heat within the sample volume is carried both by radiation and conduction, requiring appropriate adjustments to data processing in laser flash analysis. In experiments where a high-emissivity coating is applied to both faces of a semi-transparent sample, an unconstrained diathermic model is conventionally used, allowing to separate conductive and radiative heat fluxes. At high temperatures, materials with strong anisotropic scattering produce a sharp initial peak on the temperature curve, which this simple model fails to reproduce. A more complex coupled radiative–conductive problem needs to be considered instead. Although the general methods for solving radiative transfer problems had been formulated many decades ago, their numerical implementation is not always straightforward. This paper presents the complete set of algorithms for solving the coupled problem allowing to increase the measurement accuracy. The constituent numerical techniques are cross-verified, and the computational method is validated on a set of experimental data collected from a synthetic alumina sample.

1. Introduction

High-temperature measurements of thermal properties [1,2] can be challenging for many reasons, including purely instrumental ones [3]. In laser flash analysis, samples are illuminated with a pulsed laser, which induces a thermal gradient. This, in turn, creates heat fluxes acting to return the material back to thermal equilibrium. Monitoring the changes in temperature distribution allows inferring the parameters controlling this process, such as thermal diffusivity (conductivity). Samples transparent to incident radiation are coated with thin layers of gold or graphite [4]. For obvious reasons, gold coatings can only be applied in a limited temperature range. Using graphite does not impose this limitation — however, the measurement procedure has to account for both the conductive and radiative heat fluxes within the sample material. This increases the mathematical complexity of the problem, now also linked to the material optical properties. Measurements conducted with metal oxides [5,6], including oxide nuclear fuel [7], or non-metals, e.g. thermal barrier coatings [8], have proven to be difficult, since they require a dedicated data processing method correctly accounting for the bimodal thermal transfer. The non-vanishing interest in accurately measuring thermal properties of semi-transparent materials has instigated the development of mathematical methods aimed at quantifying radiative transfer and its coupling with heat conduction. Although some authors focused on delivering quick estimates based on non-coupled heat conduction and radiative transfer [9–12], significant effort has been undertaken to address the coupled problem in laser flash analysis, primarily based on the works [13–16] with a recent development reported by Braiek et al. [17]. These models consider radiative transfer in either non-scattering or weakly-scattering media. In the latter case, approximate solutions to the radiative transfer equation (RTE) are based on the exponential kernel technique or the two-flux method. These techniques, widely used in the past [18], may yield unrealistic results when the scattering phase function is strongly anisotropic. Moreover, simplifications are required to reach an approximate analytical solution; the heating term needs to be small compared to the ambient temperature. This is typically never satisfied under experimental conditions. To treat the radiative part, the three-flux method has also been considered in [19] and an early attempt to use the discrete ordinates method (DOM) – first introduced by Chandrasekhar [20] – was reported by da Silva et al. [21]. Currently, DOM is often applied to this kind of problems [22–24], although it is still not clear

* Corresponding author.
E-mail address: artem.lunev@ukaea.uk (A. Lunev).

https://doi.org/10.1016/j.ijthermalsci.2020.106695
Received 3 July 2020; Received in revised form 10 September 2020; Accepted 12 October 2020

Nomenclature

Constants

σ_0	Stefan–Boltzmann constant

Heat equation

l	Sample thickness
T_0	Ambient temperature
Q	Energy per laser pulse
d	Sample diameter
ε	Hemispherical emissivity
λ	Thermal conductivity
$\mathrm{Bi} = 4\sigma_0\varepsilon T_0^3 l/\lambda$	Biot number
$\delta T_m = 4Q/(C_\mathrm{p}\rho\pi d^2 l)$	Adiabatic heating
$\theta = (T - T_0)/\delta T_m$	Dimensionless heating
$T(z,t)$	Local temperature
Fo	Fourier number
a	Thermal diffusivity
F	Heat flux
$y = z/l$	Dimensionless coordinate
$\eta = \varepsilon/(2-\varepsilon)$	Diathermic coefficient

Radiative transfer

ψ	Hemispherical absorptivity
χ	Hemispherical scattering coefficient
ω_0	Single-scattering albedo
n	Refractive index
g	Scattering anisotropy
$q = F/(n^2\sigma_0 T_0^3)$	Dimensionless heat flux
$\tau_0 = l\psi$	Optical thickness
$\tau = \tau_0 y$	Optical coordinate
I, i	Intensity (dimensionless)
μ, μ'	Direction cosine of incident (scattered) rays
$\Phi(\mu,\mu')$	Scattering phase function
$J(t)$, $j(t)$	Integrated spectral radiance (dimensionless)
$N_\mathrm{P} = \lambda/(4\sigma_0 n^2 T_0^3 l)$	Planck number
$E_n(t)$	Exponential integral of the order n
S, s	Source function (dimensionless)

Discrete methods

Δt	Fo increment (time step)
Λ	Second-order difference operator
Est, **est**	Error estimators
ω_R	Relaxation parameter
ϕ	Discrete flux derivative
σ	Scheme weight
τ_F	Time step factor
ξ_j	Grid point
$a_{nn'}$, b_n, $\widehat{b}_n$, c_n	Butcher tableau coefficients
$atol$	Absolute error tolerance
e_it	Relaxation error tolerance of iterative solution
f	Right-hand side (RTE)
h	Uniform grid step
h_l	Adaptive grid step
L	Central-difference operator
M	Number of quadrature nodes
N	Number of spatial grid points
$rtol$	Relative error tolerance
s_G	Stretching factor
t	Discrete optical coordinate
w	Quadrature weights

Subscripts

j	Spatial index (heat equation)
l	Spatial index (DOM)
m, m'	Angular indices (DOM)

Superscripts

$\widehat{\ }$	Value at previous time step
i	Time step number
k, u	Iteration numbers
n, s	Stage number

Abbreviations

(E)SDIRK	(Explicit First Stage) Single Diagonally Implicit Runge–Kutta
BS23	Bogacki–Shampine (3,2) Solver
DOM	Discrete Ordinates Method
DP5	Dormand–Prince (5,4) Solver
FE (FTCS)	Fully-Explicit Scheme (Forward Time Centred Space)
FI	Fully-Implicit Scheme
RTE	Radiative Transfer Equation
SI	Semi-Implicit Scheme
TR-BDF2	Trapezoidal Rule with Second-Order Backward Differencing

if using the traditional implementation of DOM [25,26] has indeed increased the reliability of laser flash analysis for semi-transparent samples; in some cases the determination of optical properties can be difficult [27]. Typically [28,29], DOM combines either a trapezoidal implicit integrator or even an explicit step method (when scattering can be neglected) with a level-symmetric quadrature proposed by Lathrop and Carlson [30]. The main issues behind angular and spatial discretisation have been previously reported in [31,32]. When applied to one-dimensional problems, the standard combination is not always optimal, for instance, due to the inherent stiffness of the problem and the negative weights produced by higher-order quadratures. In the majority of cases though, the manufacturers of equipment for laser flash analysis still supply software implementing only simplified non-coupled models for experimental data treatment [33]. The commercial software is intended for use as a black box, with no means of verifying the calculation uncertainty associated with the use of a specific model. Hence, the model choice still remains somewhat a matter of personal taste. This paper is aimed at delivering reliable and fast numerical algorithms for one-dimensional coupled conductive–radiative heat transfer with application to the laser flash analysis, which lack the limitations stated above. The algorithm and procedures outlined in this work are part of the PULsE (**P**rocessing **U**nit for **L**aser Fla**s**h **E**xperiments) software, which is an open-source, cross-platform Java code freely distributed under the Apache 2.0 license [34].

2. Diathermic medium bounded by grey walls

2.1. Problem statement

Early models used in laser flash measurements of semi-transparent samples considered radiation and conduction as non-coupled phenomena since this greatly simplified the mathematical formulation of the problem. Tischler et al. [9] considered an exponential decay of radiation intensity in a solid partially transparent to the laser pulse. McMasters et al. [10] applied the optically thick approximation and introduced an additional source term in the heat equation. These models are useful to gain a crude estimate of thermal diffusivity e.g. in porous samples and semi-conductors with an intermediate band gap. Rather than considering laser penetration in solids – a complex problem associated with the diffusion of charge carriers, their re-combination and thermalisation by phonon emission [35] – it is much easier to manually restrict the laser absorption depth by applying a graphite coating. Blumm et al. [11] proposed the diathermic model specifically to deal with this case; an analytical solution was later developed by Mehling et al. [12]. A variation of this model is currently used in software packaged with some commercial instruments and is directly incorporated into the patented measurement procedure [36]. Hence, the problem statement and the numerical solution needed to be developed from scratch.

The diathermic model is based on the following propositions:

(a) A cylindrically shaped sample is completely transparent to thermal radiation;
(b) The front (laser-facing) and rear (detector-facing) sides of the sample are coated by a thin grey absorber;
(c) The coatings are in perfect thermal contact with the bulk material;
(d) The side surface is free from any coating.

Consequently, the monochromatic laser radiation is largely absorbed at the front face of the sample ($y = 0$), causing immediate heating. A portion of thermal radiation causes the rear face ($y = 1$) to start heating precisely at the same time (ahead of thermal conduction). The remainder energy dissipates in the ambient. It is thus sufficient to consider three radiative heat fluxes. The first two correspond to heat dissipation within the furnace chamber [3]. The third flux acts to thermalise the parallel boundaries by radiative transfer only [37]:

$$F_{0\to\infty} \approx \varepsilon\sigma_0 \left(T^4(0,t) - T_0^4\right), \tag{1a}$$

$$F_{1\to\infty} \approx -\varepsilon\sigma_0 \left(T^4(l,t) - T_0^4\right), \tag{1b}$$

$$F_{1\to 2} \approx \frac{\varepsilon}{2-\varepsilon}\sigma_0 \left(T^4(0,t) - T^4(l,t)\right), \tag{1c}$$

where F denotes the heat flux, l is the sample thickness, T_0 is the initial (ambient) temperature, and the emissivities of both faces are assumed to be equal ($\varepsilon_1 = \varepsilon_2 = \varepsilon$).

Let $\eta = \varepsilon/(2-\varepsilon)$, so that $0 < \eta \le 1$. Since nonlinear heat losses can be neglected [Appendix A], the boundary problem is written as:

$$\frac{\partial\theta}{\partial \mathrm{Fo}} = \frac{\partial^2\theta}{\partial y^2}, \quad 0 < y < 1, \quad \mathrm{Fo} > 0, \tag{2a}$$

$$\left.\frac{\partial\theta}{\partial y}\right|_{y=0} = \mathrm{Bi}\cdot\theta_{y=0} + \eta\mathrm{Bi}\cdot(\theta_{y=0} - \theta_{y=1}) - \Phi(\mathrm{Fo}), \tag{2b}$$

$$\left.\frac{\partial\theta}{\partial(-y)}\right|_{y=1} = \mathrm{Bi}\cdot\theta_{y=1} + \eta\mathrm{Bi}\cdot(\theta_{y=1} - \theta_{y=0}), \tag{2c}$$

$$\theta(0,y) = 0, \tag{2d}$$

where Eqs. (2a) and (2d) and the corresponding notations are the same as in [3]. The standard non-dimensional variables are used (defined in Appendix A): Bi is the Biot number indicative of heat loss, Fo is the Fourier number (dimensionless time), $\theta = \theta(y, \mathrm{Fo})$ and $\Phi(\mathrm{Fo})$ are the temperature and laser pulse functions — also dimensionless.

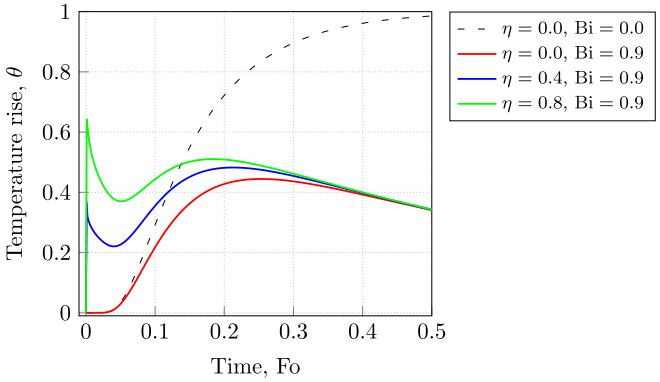

Fig. 1. An example calculation using the diathermic model (Section 2.1) at different Bi and η values. The radiative terms in Eqs. (2b) and (2c) cause significant deviation from the classical behaviour.

2.2. A finite-difference solution

Let the superscript i and the subscript $j = 0, \ldots, N-1$ denote the time step and the coordinate index respectively. The boundary conditions [Eqs. (2b) and (2c)] are expressed in finite differences as follows:

$$L\theta_0 = \mathrm{Bi}\cdot\theta_0 + \eta\mathrm{Bi}\cdot(\theta_0 - \theta_{N-1}) - \widetilde{\Phi}^{i+1}, \tag{3a}$$

$$-L\theta_{N-1} = \mathrm{Bi}\cdot\theta_{N-1} + \eta\mathrm{Bi}\cdot(\theta_{N-1} - \theta_0), \tag{3b}$$

The usual Taylor expansion is written down in the h-vicinity of $\xi = \xi_0$ and $\xi = \xi_{N-1}$, thus defining the virtual nodes $\xi = \xi_{-1}$ and $\xi = \xi_N$ needed to evaluate the boundary derivatives. After some elementary algebra, an $O(h^2 + \Delta t)$ accurate scheme is readily obtained:

$$\theta_0^{i+1}\left[1 + h^2/(2\Delta t) + h\mathrm{Bi}(1+\eta)\right] - \theta_1^{i+1} - \theta_N^{i+1}h\eta\mathrm{Bi} = h^2/(2\Delta t)\theta_0^i + h\Phi^{i+1}, \tag{4a}$$

$$\theta_{N-1}^{i+1}\left[1 + h^2/(2\Delta t) + h\mathrm{Bi}(1+\eta)\right] - \theta_{N-2}^{i+1} - \theta_0^{i+1}h\eta\mathrm{Bi} = h^2/(2\Delta t)\theta_{N-1}^i, \tag{4b}$$

with the heat equation also given in finite differences:

$$a_j\theta_{j-1}^{i+1} - b_j\theta_j^{i+1} + c_j\theta_{j+1}^{i+1} = R_j, \tag{5}$$

where $a_j = c_j = 1$. A fully implicit scheme shown previously to work well in most cases [3] corresponds to: $b_j = 2 + h^2/\Delta t$, $R_j = -h^2/\Delta t\,\theta_j^i$.

Note that Eqs. (4a) and (4b) contain reference to θ_{N-1} and θ_0 respectively, which prevents from applying the standard solution scheme [3]. The set combining Eqs. (4) and (5) is reduced to a system of linear equations expressed in a matrix form. The corresponding matrix is composed of an inner tridiagonal block and a border formed by an extra row and column. This block system is solved using the Sherman–Morrison–Woodbury identity [38] and the Thomas algorithm [39] for the main block. An example calculation is shown in Fig. 1. The input parameters include a default grid density $N = 30$ and a time step $\Delta t = t_F h^2$, where $t_F = 0.5$ is a factor ensuring numeric stability.

3. The general form of the coupled conductive–radiative heat transfer problem

The following is the equation of radiative transfer in a plane-parallel geometry with an axially symmetric radiation field for a grey participating (i.e., emitting, absorbing, and scattering) medium compliant with the Kirchhoff's law [40]:

$$\frac{dI}{ds} = -(\psi + \chi)I + \psi J + \chi\int_{\mu'} I\Phi(\mu,\mu')\frac{\mathrm{d}\mu'}{2}, \tag{6}$$

$$J = J(\tau) = \frac{n^2\sigma_0 T^4(\tau)}{\pi} = \frac{n^2\sigma_0 T_0^4}{\pi}\left(\frac{T(\tau) - T_0}{T_0} + 1\right)^4,$$

where s is the path travelled by radiation; n is the refractive index of the medium; ψ, χ and ε are respectively the linear absorption coefficient, the scattering coefficient and the emissivity — all averaged over the radiation spectrum; $\Phi(\mu,\mu')$ is the phase function of scattering, such that $\int \Phi(\mu,\mu')d\mu'/2 = 1$; $\mu = \cos\Theta$ is the cosine of the angle between the light propagation direction and the outward normal to an elementary illuminated surface.

It is convenient to express Eq. (6) in terms of the optical thickness $\tau = \int \psi \, \mathrm{d}s = \int \psi \, \mathrm{d}y/\cos\Theta$, which then allows separating the positive ($0 < \mu \leq 1$) and negative ($-1 \leq \mu < 0$) streams. After introducing the albedo for single scattering $\omega_0 = \chi/(\psi + \chi)$, the RTE e.g. for I^+ takes the form:

$$\mu\frac{\partial I^+}{\partial \tau} + I^+ = S(\tau,\mu), \quad 0 < \mu \leq 1, \tag{7}$$

where the source function is defined as $S(\tau,\mu) = (1-\omega_0)J + 0.5\omega_0 \int_{\mu'} I\Phi(\mu,\mu')\mathrm{d}\mu'$.

A matching equation may be written for I^-, thus the RTE may be solved separately for streams propagating in the positive and negative hemisphere originating at either $\tau = 0$ or at $\tau = \tau_0 := l\psi$. The complexity of the problem is determined by the source function $S(\tau,\mu)$, which in some cases, e.g. at $\omega_0 = 0$, allows an analytical solution. Once a solution has been obtained, the net radiative heat flux $F(\tau)$ can be calculated using an expression for a radiative field with axial symmetry [20]:

$$F(\tau) = 2\pi\int_{-1}^{1} I(\mu,\tau)\mu d\mu = 2\pi\left[\int_0^1 I^+(\mu)\mu\mathrm{d}\mu - \int_0^1 I^-(-\mu)\mu\mathrm{d}\mu\right], \tag{8}$$

Conduction and radiation both contribute to the heat flow, which becomes

$$-\frac{\lambda}{l}\frac{\partial T}{\partial y} + F(\tau_0 y)$$

In the isotropic case $dF/dy = \tau_0 \times dF/d\tau$ and the dimensionless heat equation may be written as:

$$\frac{\partial\theta}{\partial \mathrm{Fo}} = \frac{\partial^2\theta}{\partial y^2} + \frac{\tau_0}{N_\mathrm{P}} \times \left(-\frac{dq}{d\tau}\right), \tag{9a}$$

$$\left.\frac{\partial\theta}{\partial y}\right|_{y=0} = \mathrm{Bi}\cdot\theta - \Phi(\mathrm{Fo}) + \frac{1}{N_\mathrm{P}}q(0), \tag{9b}$$

$$\left.\frac{\partial\theta}{\partial y}\right|_{y=1} = -\mathrm{Bi}\cdot\theta + \frac{1}{N_\mathrm{P}}q(1), \tag{9c}$$

$$\theta(0,y) = 0. \tag{9d}$$

where $q = F/(n^2\sigma_0 T_0^3)$ is the dimensionless radiative flux; in addition, the Planck number is introduced: $N_\mathrm{P} = \lambda/\left(4\sigma_0 n^2 T_0^3 l\right)$. The renormalisation of the heat flux simply leads to substituting the emission function $J(\tau)$ [Eq. (7)] with

$$j(\tau) = \frac{1}{4\pi}\frac{T_0}{\delta T_\mathrm{m}}\left[1 + \theta\left(\tau/\tau_0\right)\frac{\delta T_m}{T_0}\right]^4, \tag{10}$$

which is also dimensionless.

The boundary radiative fluxes $q(0)$ and $q(1)$ are inferred from the boundary intensities $I^+(0)$ and $I^-(\tau_0)$ determined through the conditions of diffuse emission and reflection [e.g. [41]]:

$$I^+(0) = \varepsilon J(0) + (1-\varepsilon)G_0/\pi, \tag{11a}$$

$$I^-(\tau_0) = \varepsilon J(\tau_0) + (1-\varepsilon)G_{\tau_0}/\pi, \tag{11b}$$

where G_0 and G_{τ_0} is the incident irradiation reaching the respective boundary.

4. A closer look at the radiation problem

4.1. Useful special cases

4.1.1. Exact solution at $\omega_0 = 0$

In the absence of scattering, the source function $s(\tau,\mu)$ is simply equal to the emission function $j(\tau)$. This then simplifies the equation, which is solved in terms of the exponential integrals $E_n(t)$ (see e.g. [40]). The latter are defined as $E_n(t) = \int_0^1 e^{-t/\mu}\mu^{n-2}\mathrm{d}\mu$, $n > 0$. This leads to the following expression for the radiative flux [42]:

$$q(\tau) = 2\pi i^+(0)E_3(\tau) - 2\pi i^-(\tau_0)E_3(\tau_0-\tau) + 2\int_0^\tau \pi j(t)E_2(\tau-t)dt - 2\int_\tau^{\tau_0}\pi j(t)E_2(t-\tau)dt, \tag{12a}$$

where $i^+(0)$ and $i^-(0)$ are the boundary intensities.

Consequently, the radiation fluxes at the boundaries are:

$$q(0) = \pi i^+(0) - 2\pi i^-(\tau_0)E_3(\tau_0) - 2\int_0^{\tau_0}\pi j(t)E_2(t)\mathrm{d}t, \tag{13a}$$

$$q(\tau_0) = -\pi i^-(\tau_0) + 2\pi i^+(0)E_3(\tau_0) + 2\int_0^{\tau_0}\pi j(t)E_2(\tau_0-t)\mathrm{d}t. \tag{13b}$$

Combining Eqs. (11) and (13) allows to evaluate $i^+(0)$ and $i^-(\tau_0)$ from a set of two linear equations (see e.g. [13]):

$$i^+(0) = \frac{C_1 + DC_2}{1-D^2}, \quad i^-(\tau_0) = \frac{C_2 + DC_1}{1-D^2}, \tag{14a}$$

$$C_1 = \varepsilon j(0) + 2(1-\varepsilon)\int_0^{\tau_0} j(t)E_2(t)\mathrm{d}t, \tag{14b}$$

$$C_2 = \varepsilon j(\tau_0) + 2(1-\varepsilon)\int_0^{\tau_0} j(t)E_2\left(\tau_0 - t\right)\mathrm{d}t, \tag{14c}$$

$$D = 2(1-\varepsilon)E_3(\tau_0). \tag{14d}$$

The heat source term in Eq. (9) can either be calculated using a discrete approximation or exactly using the analytic expression below derived using the properties of the exponential integral (the reader is referred to [40]):

$$\left(-\frac{dq}{d\tau}\right) = 2i^+(0)E_2(\tau) + 2i^-(\tau_0)E_2\left(\tau_0-\tau\right) - 4j(\tau) + 2\int_0^{\tau_0} j(t)E_1(|\tau-t|)\mathrm{d}t \tag{15}$$

A quadrature scheme needs to be used in order to calculate the integrals in Eqs. (12) and (15) – this is given in Appendix B.

4.1.2. The two-flux approximation

For a weakly-anisotropic phase function $\Phi(\mu,\mu')$, when τ_0 is not very large, the two-flux approximation originally introduced by Schuster [43] and Schwartzschild and Gesell [44] has been shown to yield sufficiently accurate results [45]. In current notations, this approximation considers I^+ and I^- averaged over the positive and negative hemispheres correspondingly. The governing equations are then [46]:

$$\frac{dI^+}{d\tau} = -2I^+[1-(1-u)\omega_0] + 2\omega_0 u I^- + 2(1-\omega_0)\pi J(\tau), \tag{16a}$$

$$\frac{dI^-}{d\tau} = -2I^-[1-(1-u)\omega_0] + 2\omega_0 u I^+ + 2(1-\omega_0)\pi J(\tau), \tag{16b}$$

where u is an integral scattering parameter of the model.

The phase function can be expanded in a series of Legendre polynomials [20]. In the linear-anisotropic approximation the series is truncated after the second term, which in a axially-symmetric radiation field gives rise to $\Phi(\mu,\mu') = 1 + g\mu\mu'$. This corresponds to $u = 0.5$–$0.25g$.

4.2. The general case of strong anisotropic scattering in a nonlinear grey participating medium

The true multi-modal [47] form of the scattering function $\Phi(\mu,\mu')$ can be derived from the Lorenz–Mie theory (see e.g. [48]). In most practical applications, it is more convenient to use an approximation, which still captures the strongly anisotropic scattering behaviour. This is commonly done using the single-parameter Henyey–Greenstein phase function [49]. Other specialised functions have been discussed in [50–53].

The phase function of interest is thus:

$$\Phi(\mu,\mu') = (1-g^2)(1+g^2-2g\mu\mu')^{-3/2}. \tag{17}$$

If the integral over $\Phi(\mu,\mu')$ in Eq. (6) cannot be simplified, as in case of $\Phi(\mu,\mu')$ given by Eq. (17), the solution to the RTE becomes quite involved. Some effort in solving the RTE and, indeed, the coupled problem has been undertaken by many authors [25,26,54]. Generally, the discrete ordinates method (DOM) is used for this purpose. Henceforth, the paper is focused on the numerical implementation of DOM.

Recall the general form of the source function:

$$s(\tau,\mu)=(1-\omega_0)j(\tau)+\frac{\omega_0}{2}\int_{-1}^{1} i(\tau,\mu)\Phi(\mu,\mu')d\mu \tag{18}$$

The idea behind DOM is to evaluate the integral on the right-hand side using a quadrature rule. A discrete set of nodes is introduced: μ_m, $m=0,\dots,M-1$, with an equal number of negative and positive nodes; each node is assigned a certain weight w_m. The discrete form of Eq. (18) is:

$$s_m=(1-\omega_0)j(\tau)+\frac{\omega_0}{2}\sum_{m'=0}^{M-1} i_{m'}\Phi(\mu_m,\mu_{m'})w_{m'}\mu_{m'}. \tag{19}$$

The discrete RTE [Eq. (7)] is given by:

$$\mu_m\frac{\partial i_m}{\partial\tau}+i_m=s_m \tag{20}$$

with the boundary conditions of diffuse emission and reflection [Eq. (11)]:

$$i_m(0,\mu_m>0)=\varepsilon j(0)-2(1-\varepsilon)\sum_{\mu_{m'}<0} i_{m'}\mu_{m'}w_{m'} \tag{21a}$$

$$i_m(\tau_0,\mu_m<0)=\varepsilon j(\tau_0)+2(1-\varepsilon)\sum_{\mu_{m'}>0} i_{m'}\mu_{m'}w_{m'} \tag{21b}$$

The net radiative flux [Eq. (12)]:

$$q(\tau)=2\pi\sum_{m=0}^{M-1} i_m\mu_m w_m. \tag{22}$$

5. The solution to the heat problem

It is convenient to first select an appropriate numerical scheme for solving the heat problem outlined in Section 3 before launching a full-scale analysis of the radiative transfer problem (Section 4.2). For this reason, the analytical solution obtained in Section 4.1.1 is used to calculate the heat fluxes q and their derivatives $dq/d\tau$ (for details of the calculation method the reader is referred to Appendix B). The current section includes a comparison of various finite-difference scheme for solving the heat problem.

5.1. The family of finite-difference schemes

The problem can be solved using finite difference schemes with an embedded fixed-point iteration algorithm. In this section, a rectangular grid $\xi_j=j/(N-1)$, $j=0,\dots,N-1$ is assumed with a time step $\Delta t=t_F h^2$, where $0<t_F\le 1$. Let $\widehat{\theta}_j$ be the temperature value at the previous timestep. Further, let the second-order differential operator be defined as $\Lambda\theta_j=\left(\theta_{j+1}-2\theta_j+\theta_{j-1}\right)/h^2$. The discrete heat equation is then written as follows [39]:

$$\frac{\overset{k+1}{\theta}_j-\widehat{\theta}_j}{\Delta t}=\left(\sigma\Lambda\overset{k+1}{\theta}_j+(1-\sigma)\Lambda\widehat{\theta}_j\right)+\frac{\tau_0}{N_{\mathrm{P}}}\overset{k}{\phi}_i, \tag{23}$$

where $0\le\sigma\le 1$ is the weight of the scheme; ϕ_j is some finite-difference representation of the term $(-dq/dt)$.

Special cases of Eq. (23) include the fully-explicit (FE) scheme at $\sigma=0$, also known as the forward-time centred-space (FTCS), and the fully-implicit (FI) scheme at $\sigma=1.0$. Schemes with intermediate weights ($0<\sigma<1$) are colloquially referred to as semi-implicit (SI).

The FE scheme allows to calculate the reduced temperature θ_j at $j=1,\dots,N-2$ using an explicit formula. Its implementation is straightforward.

Both the FI and SI schemes follow a different solution logic (see Appendix A where a more detailed description of the general algorithm is presented). After some elementary algebra, the following expressions are derived for the coefficients used in the tridiagonal matrix algorithm:

$$\overline{\alpha}_1=\frac{2\Delta t\sigma}{h^2+2\Delta t\sigma(1+h\mathrm{Bi})}, \tag{24a}$$

$$\overline{\beta}_1=\frac{2\Delta t h(\sigma\Xi+(1-\sigma)\widehat{\Xi}-\sigma q_0/N_{\mathrm{P}}-(1-\sigma)\widehat{q}_0/N_{\mathrm{P}})}{h^2+2\Delta t\sigma(1+h\mathrm{Bi})}+\frac{h^2(\widehat{\theta}_0+\tau_0\phi_0\Delta t/N_{\mathrm{p}})+2\Delta t(1-\sigma)\left[\widehat{\theta}_1-\widehat{\theta}_0(1+\mathrm{Bi}\cdot h)\right]}{h^2+2\Delta t\sigma(1+h\mathrm{Bi})}, \tag{24b}$$

$$\theta_{N-1}=\left\{\sigma\overline{\beta}_{N-1}+\frac{h^2}{2\Delta t}\widehat{\theta}_{N-1}+\tau_0h^2\phi_{N-1}/(2N_{\mathrm{p}})+(1-\sigma)\left[\widehat{\theta}_{N-2}-\widehat{\theta}_{N-1}(1+h\mathrm{Bi})\right]+\frac{h}{N_{\mathrm{P}}}\left[\sigma q_{N-1}+(1-\sigma)\widehat{q}_{N-1}\right]\right\}/\left\{\frac{h^2}{2\Delta t}+\sigma(1+h\mathrm{Bi}-\alpha_{N-1})\right\}, \tag{24c}$$

where Ξ is the discretised pulse function, k is the iteration number, $\overline{\alpha}_j$ and $\overline{\beta}_j$ are the coefficients in the general relation $\theta_j=\overline{\alpha}_{j+1}+\theta_{j+1}\overline{\beta}_{j+1}$.

The scheme is solved iteratively until converged values of $\overset{k+1}{\theta}_0$ and $\overset{k+1}{\theta}_{N-1}$ are obtained (usually a few iterations are required). It is at least $O(h^4+\Delta t^2)$ accurate if [39]:

$$\phi_j^i=\frac{5}{6}\dot{q}_j^{i+1/2}+\frac{1}{12}\left(\dot{q}_{j-1}^{i+1/2}+\dot{q}_{j+1}^{i+1/2}\right), \tag{25a}$$

$$\sigma=\frac{1}{2}-\frac{h^2}{12\Delta t}, \tag{25b}$$

where the fractional index in the superscript indicates averaging over two consequent time steps and $\dot{q}=(-dq/d\tau)$ is the reversed flux derivative calculated using the specific implementation of the RTE solver.

5.2. Verification and benchmarking

The general method (Section 3) and the finite-difference schemes are verified against the reference solutions reported in [14] for $\tau_0=0.1$ and $\tau_0=100$ at $N_{\mathrm{P}}=0.8612$ and $T_0=800$ K. The calculated time–temperature profiles are shown in Fig. 2 where a good agreement between the linearised analytical case and the exact numerical solution is observed at $\delta T_{\mathrm{m}}=0.4$. Implicit schemes produce more accurate results compared to the explicit scheme; particularly, the fourth-order accurate semi-implicit scheme described in Section 5.1 performs well even for coarse grids with $N=10$. This is especially important in the light of a high demand on computational resources expected when solving the inverse coupled radiative–conductive problem. It is also evident that only a numerical scheme is applicable to solving the heat problem (9) at anywhere near realistic $\delta T_{\mathrm{m}}/T_0$ values [note the difference between Fig. 2(a) and (c)].

6. Spatial discretisation and integration

Commonly, the RTE [Eq. (20)] is integrated using a diamond-differencing scheme (see e.g. [55]), also known as the central-difference scheme, which for a one-dimensional problem is exactly the same as the implicit trapezoidal rule – a second-order accurate and A-stable [56] (i.e., stable at any step size) method. All alternative conventional methods are based on the finite-volume methodology [41,57] and include: the first-order step scheme, the second-order exponential, hybrid and CLAM schemes. Advances in spatial discretisation schemes for RTE, mainly based on NVD and TVD for multi-dimensional radiative transfer, have been reviewed in [32] – however, with no significant progress reported for high-order spatial differencing schemes. More recently, Maginot et al. [58] have used a stiffly-accurate single diagonally

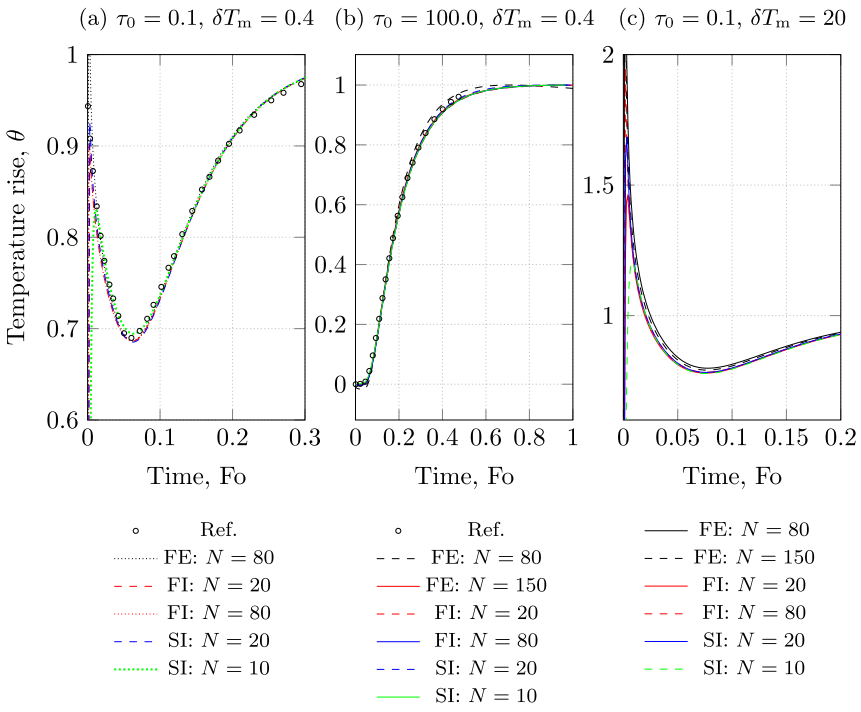

Fig. 2. Comparison of calculation results using a fully-explicit (FE), fully-implicit (FI) and semi-implicit fourth-order (SI) difference schemes with the reference analytical solutions obtained for a linearised heat equation (digitised graphs from [14]). The analytical solution is exact at $\delta T_m/T_0 = 0.4/800$ but becomes invalid at higher δT_m typical under experimental conditions.

implicit Runge–Kutta (SDIRK) method reported originally by Alexander [59]. Notable implementations of SDIRK are included in [60,61]. Despite their advantages, SDIRK methods only allow a stage-order of one [56]. Higher stage-order is useful since this strongly improves accuracy when applied to stiff problems and increases the error-estimate quality [62]. Stage-order two may be achieved with the first-stage explicit SDIRK (ESDIRK). Alternative to ESDIRK is the Rosenbrock method [56], which might be more efficient for some problems [63].

6.1. Explicit Runge–Kutta with an adaptive uniform grid

A given ODE can have varying stiffness depending on the parameter values. For the RTE, stiffness is mainly determined by τ_0. At $\tau_0 < 1$ the problem can be effectively treated as non-stiff. When stiffness is not an issue, explicit embedded Runge–Kutta schemes can be used. If high accuracy is desired, a good fourth-order scheme such as the Dormand–Prince (DP54) [64] scheme with a fifth-order error control and an extended region of absolute stability can be used. Practice shows that for the current use of the RTE, error tolerance can be high, thus a lower order embedded method might be sufficient. In this case, a third-order Bogacki–Shampine (BS32) [65] scheme with second-order error control and good stability can be used. Both schemes are FSAL (first same as last), which saves computational time, and their implementation follows the same pattern described below.

Firstly, let h_l denote the signed grid step, which is positive when approaching the right boundary and negative otherwise. The following notations are used: the intensities at each stage $n = 1, \dots, s$ are denoted as $i^{(n)}$ with the corresponding coordinate $t_l^{(n)} = t_l + h_l c_n$, where m and l stand for the angular and spatial indices respectively. Matrix elements of the Butcher tableau are denoted as $a_{nn'}$, and b_n are the coefficients at the final stage s corresponding to $t_l^{(s)} = t_l + h_l$, such that $i_{ml+1} := i_m^{(s)} = i_{ml} + h_l \sum_{n=1}^{s} f_m^{(n)} b_n$. Additionally, $\widehat{b}_n$ are the components of the error estimator. First stage is either copied from the last stage of the previous step (if available) or calculated using the derivative $f_{ml} := f_m^{(0)}$ at $\tau = t_l$.

The derivative at any stage $n = 1, \dots, s$ is expressed e.g. for the left-to-right sweep:

$$f_m^{(n)} = \frac{1}{\mu_m}\left(-i_m^{(n-1)}\left[1 - \frac{\omega_0}{2} w_m \boldsymbol{\Phi}_{mm}\right] + (1-\omega_0) j\left(t_l^{(n)}\right) + \underbrace{\frac{\omega_0}{2}\sum_{m'\neq m}^{\mu_{m'}>0} i_{m'}^{(n-1)} \boldsymbol{\Phi}_{mm'} w_{m'}}_{\text{outward}} + \underbrace{\frac{\omega_0}{2}\sum_{m'\neq m}^{\mu_{m'}<0} i_{m'l+c_n} \boldsymbol{\Phi}_{mm'} w_{m'}}_{\text{inward}}\right). \tag{26}$$

where $i_m^{(n)} = i_{ml} + h_l \sum_{n'=1}^{n-1} a_{nn'} f_m^{(n')}$ are the outward intensities at the node m and stage n. Depending on whether the RTE is solved left-to-right or right-to-left, the angular index m for the outward intensities will run through the indices of either positive or negative nodes (cosines). For the sum over outward intensities, the latter are expressed in the same way using the solution $i_{m'}^{(n-1)}$ at the stage $n-1$. Inward intensities $i_{m'l+c_n}$ are not known *a priori*, which is why the RTE is solved iteratively; this will be described in more detail later in the text. For now these intensities are assumed to be known.

Once the derivative $f_m^{(n)}$ becomes known, it is then used to calculate the next stage approximation $i_m^{(n)}$, and so on. This process repeats for all $n = 1, \dots, s$. As soon as all derivatives have been calculated, the intensities i_{ml+1} may be evaluated using the respective expression. Error control is achieved by evaluating the vector **est**, the components of which are given by:

$$\mathrm{est}_m = h \sum_{n=1}^{s} (b_n - \widehat{b}_n) f_m^{(n)}, \tag{27}$$

where m runs through the indices of outward intensities.

Absolute and relative tolerances are introduced according to Hairer et al. [66] so that the error threshold is defined via:

$$e_{l\pm1} = atol + \max_m\left(|i_{ml}|, |i_{ml\pm1}|\right) \times rtol. \tag{28}$$

Thus, $\max_m(\mathrm{est}_m)$ is compared at each subsequent integration step $l \pm 1$ against $e_{l\pm1}$ – if the former is greater than the latter, integration stops immediately, triggering a grid re-construction with a different

segmentation: $N^{[u+1]} = s_G N^{[u]}$ (typically $s_G = 1.5$), where $[u]$ indicates the value at current iteration.

As mentioned above, to solve the RTE, one must calculate the intensities corresponding to both the negative and positive μ_m. However, when using the method above to solve either of the Cauchy problems, only half of the intensities is readily calculated while the other half is assumed to be known. To solve the RTE for all μ_m, an iterative solution is required. Here two techniques are considered [38]: the fixed-point iterations and the successive over-relaxation. In both cases, the intensities at iteration $[u+1]$ are expressed as:

$$i_{ml}^{[u+1]} = (1-\omega_R) i_{ml}^{[u]} + \omega_R i_{ml}, \tag{29}$$

where the relaxation parameter $\omega_R = 1$ for fixed-point iterations and $1 < \omega_R < 2$ in the successive over-relaxation technique. The second term on the right-hand side is the solution of the ODEs times the relaxation parameter. For instance, at $\omega_R = 1.7$ and for pure isotropic scattering at $\omega_0 = 1$, convergence is reached two times faster than for fixed-point iterations.

The stopping criterion for the iterative procedure regards the relative change to the boundary fluxes q_0 and q_N at the left and right boundaries correspondingly:

$$\frac{\left|q_0^{[u+1]} - q_0^{[u]}\right| + \left|q_N^{[u+1]} - q_N^{[u]}\right|}{\left|q_0^{[u]} + q_N^{[u]}\right|} < e_{\text{it}}, \tag{30}$$

where e_{it} is a relative error tolerance (typically, $e_{\text{it}} \simeq 10^{-4}$).

6.2. TR-BDF2 with an adaptive stretching grid

For moderately- and highly-stiff problems, e.g. at $\tau_0 > 10$, the use of a uniform grid requires a very small step size h_l to make the scheme stable, thus greatly increasing the computational cost of an explicit method. Hence, an adaptive step-size control should be used instead, which achieves true flexibility in the A/L-stable, stiffly-accurate methods, for instance, the TR-BDF2 scheme [67]. The latter can be regarded as a major improvement over the original diamond-differencing scheme for plane-parallel radiative transfer problems, since it includes the same trapezoidal rule (diamond-differencing) at the second stage and uses second-order backward-differencing at the third stage, resulting in stiff accuracy. Furthermore, it provides an asymptotically correct error estimate and allows dense output. TR-BDF2 can be regarded as an ESDIRK scheme [62].

The explicit first stage is calculated in the same way as in Section 6.1, noting that TR-BDF2 is also FSAL. The second and third stages are implicit by definition. However, because the ODEs in the DOM are linear, the corresponding intensities can easily be found explicitly from the solution of the following linear set. For instance, the left-to-right sweep at the second stage:

$$i_m^{(2)}\left[1 + \frac{h_l d}{\mu_m}\left(1 - \frac{\omega_0}{2} w_m \boldsymbol{\Phi}_{mm}\right)\right] - \underbrace{\frac{h_l d}{\mu_m}\frac{\omega_0}{2}\sum_{m'\neq m}^{\mu_{m'}>0} i_{m'}^{(2)} \boldsymbol{\Phi}_{m'm} w_{m'}}_{\text{outward}} =$$

$$i_{ml} + h_l d\, f_m^{(1)} + \frac{h_l d}{\mu_m}\left[(1-\omega_0) j(t_l + \gamma h_l) + \underbrace{\frac{\omega_0}{2}\sum_{m'\neq m}^{\mu_{m'}<0} i_{m'l+\gamma} \boldsymbol{\Phi}_{m'm} w_{m'}}_{\text{inward}}\right], \tag{31}$$

where $\gamma = 2 - \sqrt{2}$ and $d = \gamma/2$ [67].

Clearly, this reduces to a linear matrix equation $\mathbf{A}\mathbf{i}_{ml+\gamma}^{(2)} = \mathbf{B}_{ml+\gamma}^{(2)}$, which is solved by matrix inversion. Due to the $\mathbf{A}$ matrix usually being low-dimensional (the dimension is equal to a half of the total number of quadrature points), a fast matrix inversion routine has been implemented for the typical quadrature sets. For higher-order quadratures, a matrix inversion tool based on either QR, LU or Cholesky decomposition of the Apache Commons Mathematics Library is used. Since the method is ESDIRK, the final third stage uses the same matrix inverse $\mathbf{A}^{-1}$. The linear set for the third (and final) stage is (left-to-right sweep):

$$\mathbf{A}\mathbf{i}_{ml+1}^{(3)} = i_{ml}\left(1 - \frac{w}{d}\right) + \frac{w}{d} i_m^{(2)} +$$

$$\frac{h_l d}{\mu_m}\left[(1-\omega_0) j(t_l + h_l) + \underbrace{\frac{\omega_0}{2}\sum_{m'\neq m}^{\mu_{m'}<0} i_{m'l+1} \boldsymbol{\Phi}_{mm'} w_{m'}}_{\text{inward}}\right], \tag{32}$$

where $w = \sqrt{2}/4$ [67] (this should not be confused with the quadrature weights w_m).

The correct error estimate [67] valid for both stiff and non-stiff problems is then simply: $\mathbf{Est} = \mathbf{A}^{-1}\mathbf{est}$, where $\mathbf{est}$ is given by Eq. (27) and [67]:

$$\widehat{\mathbf{b}}^{\mathbf{T}} = (\,(1-w)/3,\ (3w+1),\ d/3\,)\,. \tag{33}$$

The same general scheme for error control [Eq. (28)] is used.

To take advantage of the stability properties of TR-BDF2, an adaptive grid is constructed using stretching functions [68,69]. Since rapid variation of intensities is mainly expected when approaching the boundaries, it is sufficient to maintain a small step in their vicinity. The stiff solver can then use an arbitrary large step in the remainder domain. For this purpose, the grid step h_l is defined via a hyperbolic tangent function:

$$h_l = \frac{\tau_0}{2}\left[1.0 - \frac{\tanh\left\{S_g(1-2\xi_l)\right\}}{\tanh(S_g)}\right], \quad \xi_l = 1.0/N_g^{[u]}, \tag{34}$$

where $N_g^{[u]}$ is the number of segments in a uniform grid and S_g is the stretching factor.

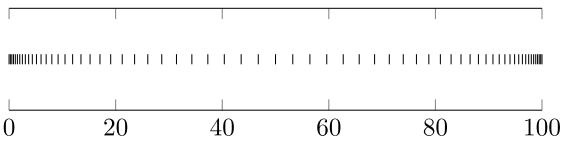

Fig. 3. A symmetric stretched grid generated using Eq. (34) at $N_g^{[u]} = 64$, $S_g = 3.0$ and $\tau_0 = 100.0$.

Fig. 3 shows an example grid generated using the above algorithm.

When the error becomes higher than the threshold given by Eq. (28), the grid is re-constructed by increasing the number of grid points in the same manner as described in Section 6.1. The first iteration always starts from a uniform grid with a default of $N_g^{[u]} = 8$ segments. The parameter S_g normally does not change during the re-construction. Finally, the same iterative procedure described in Section 6.1 is adopted to obtain convergence.

6.3. Interpolation

In each case, knowledge of the dimensionless temperature θ is required at intermediate integration steps $t^{(n)}$ used then to calculate the reduced radiance $j(t^{(n)})$. Since the temperature is defined discretely on a different external grid of the heat equation, an interpolation procedure is required to calculate the temperature θ_l at the integrator nodes. In this case, the dimensionless temperature is interpolated using natural cubic splines implemented in the Apache Commons Mathematics Library.

Both the explicit [Eq. (26)] and implicit [Eq. (31)] methods contain summation over the unknown inward intensities i_{ml+c_n}. Since all intensities are calculated at the internal grid points l and because $l + c_n$ is not a grid point, an interpolation procedure is required here as well to calculate $i_{ml+c_n}^{[u]}$ using the $i_{ml}^{[u-1]}$ values obtained at the previous

Table 1
Nodes (positive half) and weights of a G_M^{16} composite Gauss–Legendre quadrature for a function discontinuous at $\mu = 0$.

Cosine nodes, μ_m	Quadrature weights, w_m
0.980144928248767	0.050614268145189
0.898333238706814	0.111190517226691
0.762766204958165	0.156853322938942
0.591717321247824	0.181341891689181
0.408282678752176	0.181341891689181
0.237233795041834	0.156853322938941
0.101666761293186	0.111190517226693
0.019855071751233	0.050614268145190

iteration. Additionally for the implicit method, the outward intensities at the intermediate points $t_l + \gamma h_l$ are not known either, and hence the same procedure needs to be used for their calculation. Because in Runge–Kutta methods both the intensities and their derivatives are calculated, a cheap and convenient method for this interpolation is the globally C^1 Hermite interpolation described in detail in [70]. The Hermite interpolant satisfying the function and derivative values at end points of the segment $t \in [a, b]$ is:

$$h(t) = T^2(3-2T)y_1 + (T-1)^2(1+2T)y_0 + \{T^2(1-T)d_1 + (T-1)^2 T d_0\}h, \quad (35)$$

where $T = (t-a)/h_l$, $a = t_l$, $b = t_{l\pm1}$, $y_0 = i_{ml}$, $y_1 = i_{ml\pm1}$, $d_0 = f_{ml}$, $d_1 = f_{ml\pm1}$.

This allows effective interpolation of both inward and outward intensities at any intermediate point $0 < t < \tau_0$.

6.4. Angular discretisation

The quadrature choice is central to the DOM as it defines both the overall accuracy of the method and the stability requirements for the spatial integration technique. Chandrasekhar [20] originally considered the Gauss–Legendre and Lobatto (Radau) quadratures for angular discretisation. In modern calculations, the level-symmetric quadratures by Lathrop and Carlson [30] are often used [41]. These and other similar quadratures have been reviewed in [71–74]. More recently, an extensive review [75] of different quadratures has shown that for problems generating a continuous intensity field, the Gauss–Chebyshev quadrature LC11 derived by Lebedev [76] offers the highest precision. Since in many cases, particularly for the one-dimensional radiative transfer with diffuse emission and reflection conditions, the intensities are discontinuous at $\mu = 0$ (see e.g. [77]), standard quadratures which do not specifically treat the discontinuity would give inaccurate results. The level-symmetric quadratures were designed to cover both the non-continuous and discontinuous case and are applicable to a wide range of problems. However, high-order quadratures (such as S^{10}, S^{12} etc.) yield negative weights. Although quadratures such as S^8 give sufficiently accurate results in many cases, an alternative should be considered for higher-order calculations. A composite Gaussian quadrature has been considered for Fresnel boundary conditions in [78] where the angular interval was divided in three segments. A similar procedure can be performed for the diffuse emission and reflection boundaries.

Consider the M cosine nodes and weights of a Gauss–Legendre quadrature on $[0, 1]$: $\widetilde{\mu}_m$ and $\widetilde{w}_m$. The goal is to construct a composite quadrature that will work despite the intensities being discontinuous at $\mu = 0$. The $2M$ cosine nodes of this composite quadrature are then:

$$\mu_m = \frac{\widetilde{\mu}_m + 1}{2}, \quad \mu_{m+n/2} = -\frac{\widetilde{\mu}_m + 1}{2}. \quad (36)$$

with the same weights $w_m = \widetilde{w}_m$.

By construction, the composite Gaussian quadrature given by Eq. (36) is applicable to discontinuous functions at $\mu = 0$. An example G_M^{16} ordinate set proposed in this work is given in Table 1 (note this quadrature is symmetric).

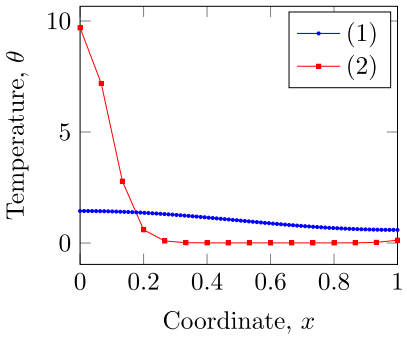

Fig. 4. Sample discrete dimensionless temperature profiles for verification and benchmarking purposes. The profiles are discretised differently to test the interpolation capability.

6.5. Verification and benchmarking

To verify the solvers and the discrete ordinate sets, two model cases were considered: (*a*) a non-scattering grey medium with diffusely emitting and reflecting walls ($\varepsilon = 0.85$, $\omega_0 = 0.0$); (*b*) an isotropic perfectly scattering medium with black walls ($\varepsilon = 1.0$, $\omega_0 = 1.0$). In the first case (Fig. 5), the DOM solution was compared against an exact analytical solution, whereas the second comparison (Fig. 6) was made in reference to the two-flux model (Section 4.1.2). The equations were solved using the GNU Octave/Matlab bvp5c solver. Two temperature profiles were used — both are shown in Fig. 4. The parameter τ_0 was allowed to vary from $\tau_0 = 0.1$ (non-stiff) to $\tau_0 = 100.0$ (very stiff).

Results for the three quadratures considered (G_M^8, S^8, G_M^{16}) show good overall agreement, with the G_M^8 and G_M^{16} quadrature producing significantly less deviation from the reference analytic solution (Fig. 5) at the boundaries (non-stiff case) and at intermediate points (stiff case). The deviation is decreased even more when a low error tolerance is selected ($rtol = 10^{-4}$, $atol = 10^{-5}$, $e_{\text{it}} = 10^{-6}$). For comparison with the two-flux model, an artificial quadrature containing two equal-weight symmetric points is examined. An exact match between the approximate analytical model and the discrete ordinates method is shown in Fig. 6, thus confirming the reliability of the numeric procedure.

Additionally, the performance of different schemes and quadratures was tested for a grey medium with a strong anisotropic scattering ($\varepsilon = 0.85$, $\omega_0 = 0.4$, $g = 0.8$). The results of different computational methods for the net fluxes shown in Fig. 7 show good mutual agreement both in the stiff and non-stiff cases.

Finally, the relative performance of different schemes was assessed in Table 2. Here the TR-BDF2 scheme in the high-tolerance mode using the G_M^8 quadrature was used as reference, corresponding to the respective 1.00 table entry. Increasing problem stiffness in the high-tolerance mode only marginally increases the computational cost for TR-BDF2. Other schemes do not perform so well in terms of performance, particularly the DP5 at $\tau_0 = 100$ is 50 times slower than the reference. BS23 performs better but still fails to deliver a reasonable computation time for stiff problems. For the G_M^{16} quadrature there was no fast matrix inversion implemented and hence the TR-BDF2 algorithm relied on a generic decomposition algorithm for the latter. This justifies the considerably more expensive calculations. Problems requiring only a small ordinates set (e.g. S^4) show a $\approx$ 1.5 increase in performance compared to the reference. Same performance for TR-BDF2 and DP5 is achieved at low error tolerance levels for a non-stiff ($\tau_0 = 0.1$) problem, whereas BS23 requires a finer step size, which almost triples the overall cost. The numbers change dramatically even for moderately-stiff problems ($\tau_0 = 10.0$), with the DP5 outperforming the BS23 scheme — as expected, since DP5 is a fourth-order method. On the other hand, both require more resources to achieve the same error tolerance compared to the TR-BDF2 due to the adaptive grid employed for the

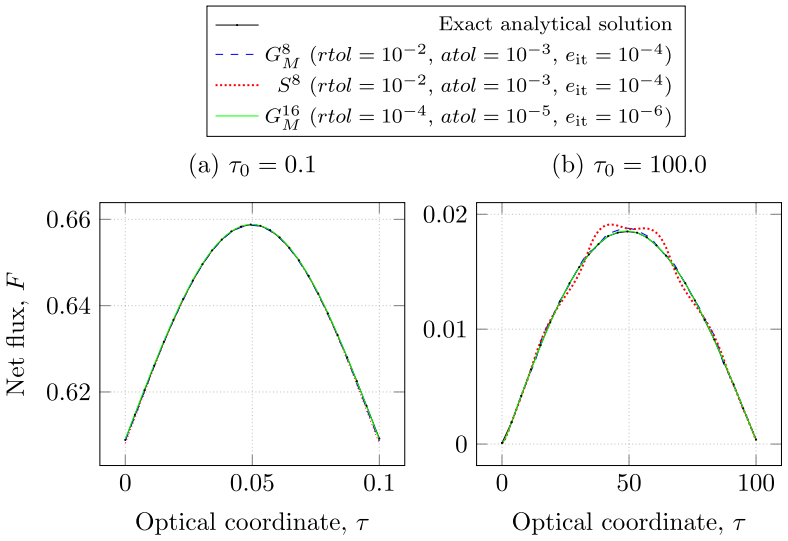

Fig. 5. Comparison of the discrete ordinates solution using a TR-BDF2 adaptive solver and different ordinate sets (G_M^8, G_M^{16}, S^8) and error tolerance levels with the exact analytical solution for a grey non-scattering medium ($\omega_0 = 0.0$, $\epsilon = 0.85$). Parameters: $\delta T_{\mathrm{m}} = 10.0$, $T_0 = 800$ K.

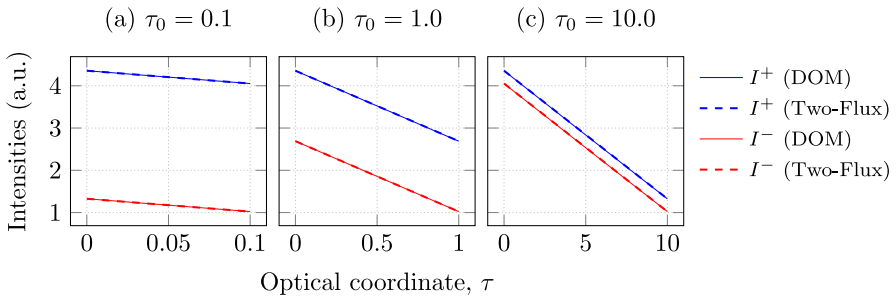

Fig. 6. Comparison of the discrete ordinates solution at low error tolerance using the TR-BDF2 solver and the G_M^8 ordinate set with the two-flux method for pure isotropic scattering in case of black walls ($\omega_0 = 1.0$, $\epsilon = 1.0$) for a test temperature profile (2). Parameters: $\delta T_{\mathrm{m}} = 36.7$, $T_0 = 800$ K. The intensities have been calculated with a re-normalised radiance $j_r = (1 + \theta \delta T_{\mathrm{m}}/T_0)^4$.

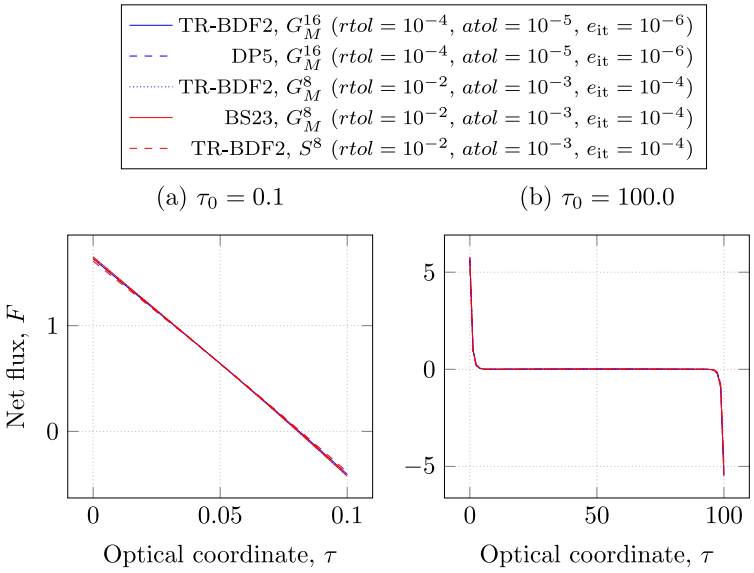

Fig. 7. Comparison between the discrete ordinates solutions using different ordinate sets (G_M^8, G_M^{16}, S^8) and solvers (BS32, DP5, TR-BDF2) at different error tolerance levels for a grey medium with a strong anisotropic scattering ($\epsilon = 0.85$, $\omega_0 = 0.4$, $g = 0.8$). Parameters: $\delta T_{\mathrm{m}} = 10.0$, $T_0 = 800$ K.

Table 2
Benchmark results of the DOM for high ($rtol = 10^{-4}$, $atol = 10^{-5}$, $e_{it} = 10^{-6}$) and low ($rtol = 10^{-2}$, $atol = 10^{-3}$, $e_{it} = 10^{-4}$) error tolerance levels using a test temperature profile at $T_0 = 800$ K and $\delta T_m = 10.0$ for strong anisotropic scattering in a grey medium ($\omega_0 = 0.4$, $g = 0.8$, $\varepsilon = 0.85$).

Error tolerance	Quadrature	Solver	Computational cost (rel.)		
			$\tau_0 = 0.1$	$\tau_0 = 10.0$	$\tau_0 = 100.0$
High	G_M^8	TR-BDF2	1.00	1.00	1.90
		DP5	1.55	6.80	50.0
		BS23	1.04	4.90	28.1
	G_M^{16}	TR-BDF2	3.76	4.95	20.0
	S^4		0.67	0.64	0.83
Low	G_M^8	TR-BDF2	1.00	4.1	9.86
		DP5	1.54	19.0	193.4
		BS23	2.84	110.5	–
	G_M^{16}	TR-BDF2	13.64	23.14	146.62
	S^4		0.85	2.30	2.475

Table 3
Test calculation parameters.

Parameter	Notation	Value	Units
Planck number	N_P	0.8612	
Scattering albedo	ω_0	0.0	
Biot number	Bi	0.1	
Test temperature	T_0	1486	K
Laser energy	Q_{las}	5	J
Specific heat	C_p	1296	J kg^{-1} K^{-1}
Density	ρ	3735	kg m^{-3}
Thermal diffusivity	a	1.254	mm^2 s^{-1}
Pulse width	t_{las}	1.5	ms
Thickness	l	1	mm
Diameter	d	10	mm

latter. For the G_M^{16} quadrature there is an expected drop in performance — and vice versa for the S^4 ordinate set.

With these results in mind, the default settings for calculation are chosen as TR-BDF2 and a G_M^8 ordinate set in the high-tolerance mode.

7. Cross-verification

The goal is to verify the complete solution to the conductive–radiative problem described in Sections 5 and 6. The specific implementation of the finite-difference schemes and the DOM equations allows treating both the absorbing–emitting medium and the participating medium without any changes to the algorithms. Therefore, it is sufficient to show the same result is obtained with DOM as previously using the exact solution for an absorbing–emitting medium (Section 4.1.1). The DOM solution in case of pure linearly-anisotropic scattering has already been verified in Section 6.5 by comparing it with the results of two-flux model (Fig. 6). Synthetic model parameters used in current verification tests are listed in Table 3. These correspond to a case of non-scattering grey medium; the latter is especially helpful since it allows an exact solution to the RTE (Section 4.1.1), examples of which have previously been shown in Fig. 2. The resulting time–temperature profiles generated by solving the boundary problem [Eq. (9)] with the radiative fluxes calculated using the discrete ordinates method were compared to similar profiles based on the analytical solution to the RTE. No deviation between the two calculation methods is observed (Fig. 8), thus indicating a correct implementation of all solvers.

8. Experimental validation

A laser flash analyser (LFA) is a machine, which utilises short laser pulses (typical durations of 0.1–5.0 ms and pulse energies 1–30 J) to create an initial thermal gradient in a sample (usually, a cylindrically shaped solid) and simultaneously measure the temperature response of a sample surface with an infrared detector [3]. Theoretically, this temperature response is fully determined by the solution of a heat problem.

Table 4
Parameter bounds and their one-to-one monotonic mapping.

Parameter, Y_i	Bounds	Mapping
Bi	$0 \le \mathrm{Bi} \le (4\sigma_0 T^3 l)/\lambda$	
N_P	$0 < N_P \le \lambda(4\sigma_0 T^3 l)^{-1}$	$Y_i = 0.5 Y_i^{\max}\left(1 + \tanh(X_i)\right)$
ω_0	$0 \le \omega \le 1$	
g	$-1 \le g \le 1$	$Y_i = \tanh(X_i)$
τ_0	$\tau_0 > 0$	$Y_i = e^{X_i}$

If the problem statement is complete and the experimental setup is performing well, a unique set of parameters exists such that the theoretical curve exactly matches the experimental measurements. Therefore, the sought values of the properties (e.g. Table 3) may be determined by conducting mathematical optimisation. The unconstrained minimisation procedure, which worked well for simpler problem statements (not involving transparency), has previously been fully described and tested in [3]. Since the experimental and calculated time sequences did not always match, a linear interpolation procedure was used to evaluate the theoretical heating at the experimentally registered time values. This enabled a simple calculation of the objective function. However, because rapid temperature variation is to be expected in experiments on semi-transparent samples, the method was further refined by extending the interpolation capability with natural cubic splines. Additionally, a simplified constrained optimisation procedure was proposed. The rationale and details for this choice are listed below.

In case of an ill-posed problem or a tendency of the computational method to fail outside a certain region in the parameter space, the unconstrained optimisation procedure will not behave well. Fig. 9 shows two almost identical time–temperature profiles obtained with two very different parameter sets. This is a classical example of an ill-posed problem [79]. To eliminate non-physical solutions, the parameter space should be bounded. The corresponding linear constraints are listed in Table 4. The complete solution of the optimisation problem with linear constraints based on the active-set method has been discussed in [80] and the general method of solving ill-posed problems is known as the Tikhonov regularisation. A very simple alternative is considered in this work mainly for demonstration purposes. A one-to-one mapping $Y_i \in \mathbb{R} \to X_i \in [a, b]$ is introduced for each parameter y_i in Table 4 using hyperbolic functions. This ensures that at each time the parameter x_i only takes 'reasonable' values. The optimisation procedure is then effectively the same, except that the search vector is formed of X_i rather than Y_i. It should also be noted that imposing these constraints is only possible if the thermal properties of the sample (specific heat and density) are known in each experiment — otherwise there is no way of telling whether the parameter value is sensible or not. As a direct consequence, this means that even the diathermic model, which does not require either the specific heat or density values for calculation, would not guarantee physically reasonable results if the thermal properties are unknown and an unconstrained optimisation is used instead.

Finally, a set of heating curves acquired from high-temperature laser flash measurements on a synthetic alumina sample ($l = 1.181$ mm) has been provided for validating the computational procedure. The LFA instrument featured: a pulsed ruby laser generating visible light at a wavelength of 694.3 nm with a pulse energy of 5 J; and a high-precision, pre-calibrated InGaAs detector with a temperature resolution of 0.02 °C. Other details of the setup have been given previously in [3,81]. The design of the sample holder is similar to that described by Lazard et al. [4]; the arrangement of the working chamber and optics is also horizontal. The difference in the sample holder designed consisted in a larger contact surface between the clamping rings and the sample. The approximate values of the pyrometer field-of-view and the laser spot were 6 mm and 8 mm respectively. The sample was coated using a graphite lacquer from a spray can.

The computational procedure used data on heat capacity and thermal expansion of alumina from [82,83]; the material density at room

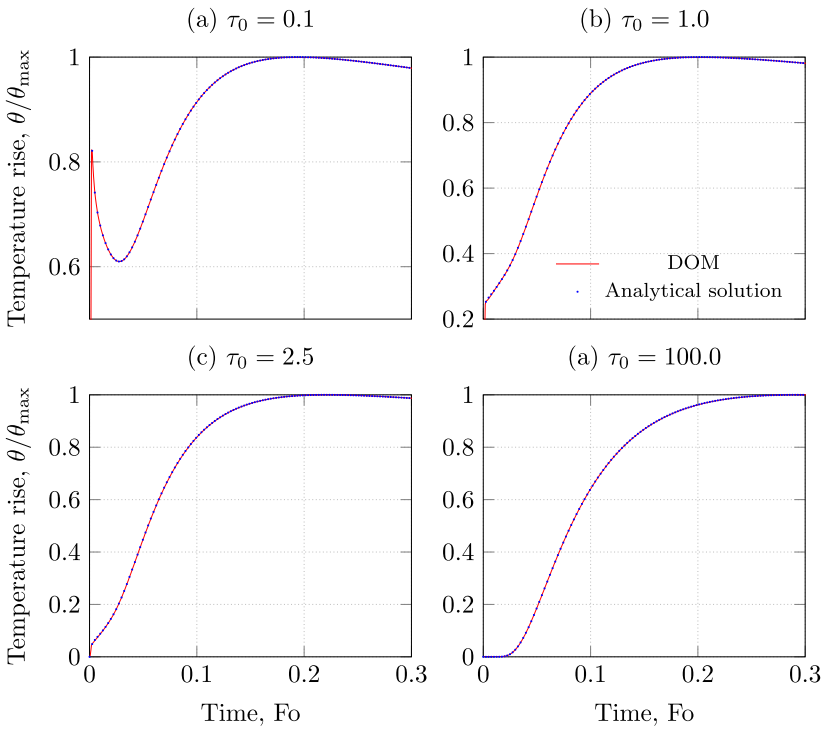

Fig. 8. Finite-difference (4th order SI scheme, $N = 16$) solutions to the heat problem with a non-scattering radiative transfer calculated using either DOM (G_M^8, TR-BDF2) or the analytical formula where a four-point Chandrasekhar's quadrature is used.

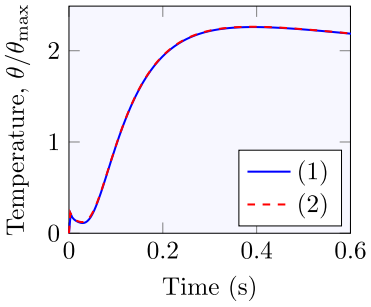

Parameter	Value	
	(1)	(2)
Bi	0.1153	0.11071
a ($\mathrm{mm^2 s^{-1}}$)	1.5314	1.48182
ω_0	0.81557	0.76694
g	0.93998	0.22385
N_P	25.48625	6.48487
τ_0	0.29264	1.55839

Fig. 9. Two seemingly equal solutions based on completely different parameter sets. The N_P parameter value in Set (1) leads to a physically impossible refractive index $n = 0.75$, whereas Set (2) yields $n = 1.48$.

temperature was measured using the hydrostatic method. Experimental data points and the optimal heating curves calculated using each of the three models discussed in this work are shown in Fig. 10. A sharp initial peak on the time–temperature profiles $\Delta T(t)$ is especially pronounced at ambient (furnace) temperatures T_0 above 1480 K. During these measurements, a pre-programmed delay of 1.25 ms between the actual laser shot and start of data acquisition was introduced (with the detector sampling interval of 0.25 ms). Therefore, it is hard to determine whether the onset of initial peak correlated with the laser pulse width (a fixed value of 1.0 ms). Results show that complete calculation with the Henyey–Greenstein phase function produced a significantly smaller deviation from the experimentally measured time–temperature profiles. Nevertheless, the deviation was still noticeable at the smallest registered times. There are several possible explanations. Firstly, the temporal shape of the laser pulse was not measured and assumed rectangular. Tests have been carried out with different simulated pulse shapes, confirming the initial peak may depend on this. Secondly, if residual graphite was left on the side surface of the sample, it could have interfered with the thermal transfer modes, resulting in an overestimation of the radiation-induced peak (graphite is significantly more conductive than alumina). Other possible factors include: imperfect alignment of the sample relative to the optical axis, non-ideal parallelism of the front and rear face of the sample — potentially causing additional reflections from the chamber walls. More validation studies are needed, which could benefit from reducing the impact of these uncertainties.

At each test temperature, thermal diffusivity (Fig. 11) was averaged over five measurements. Results show that a model fully accounting for all three processes (absorption, emission and scattering) produces systematically different values of thermal diffusivity compared to the diathermic model. The region of uncertainty (marked in red) illustrates the high sensitivity of the optimisation procedure on the initial conditions. The maximum deviation from the diathermic model is over 10%. The tendency of the optimiser to slip into a local minimum is due to the objective function being acute and multi-modal, which commonly occurs in multi-variate optimisation; moreover, even though the set of parameters can be sufficiently different, the minima are not. This highlights the necessity of introducing additional constraints — relying on e.g. the optical properties.

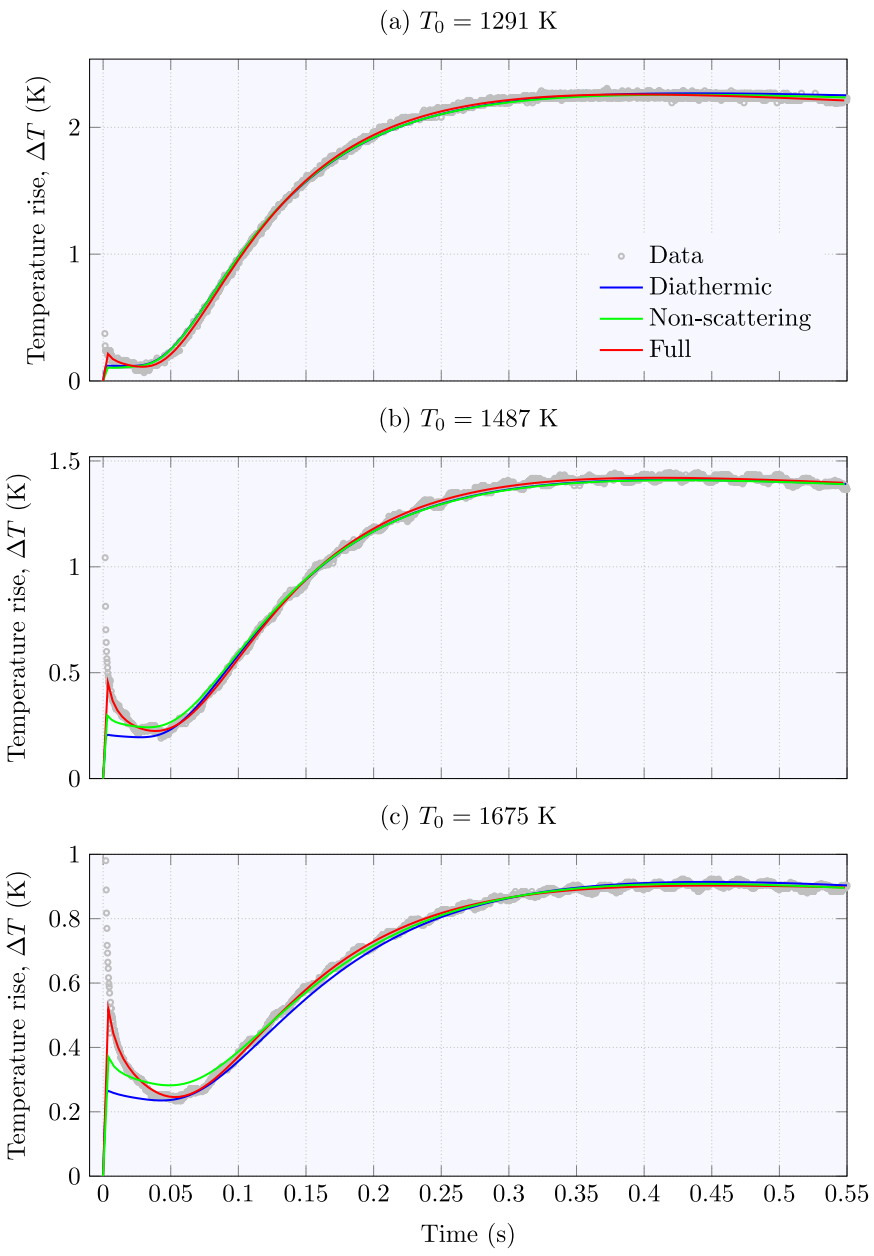

Fig. 10. Experimental rear-surface time–temperature profiles of an Al_2O_3 sample initially thermalised at three different temperatures. Shown are the optimal solutions of the simplified diathermic model and of the fully-coupled radiative–conductive model.

9. Conclusions

The numerical method described in this paper combines: (a) a stiffness-aware solver, its error control scheme and an adaptive stretching grid — specifically tailored to solving the initial value problems arising from the discretised radiative transfer equation; (b) a composite Gaussian quadrature designed to treat discontinuous intensities typical to the one-dimensional radiative transfer and (c) a fourth-order semi-implicit finite-difference scheme for numerically solving the heat problem. This combination is applied to enhance the data analysis in laser flash experiments where the material under study scatters thermal radiation anisotropically, such as when conducting measurements on transparent alumina at high temperatures. The calculation procedure reproduces the initial rapid variation of temperature typical to the strongly-scattering medium while still observing physically-reasonable values of secondary model parameters (i.e., of the optical thickness, Planck number, emissivity, scattering albedo and of the anisotropic factor). The estimate quality is benchmarked against a standard diathermic model, where the maximum deviation is observed at high temperatures and pronounced scattering anisotropy. The optimisation procedure has been modified to implement constrained search using a one-to-one mapping of the search variables. This allowed imposing realistic parameter constraints. A further refinement of the search procedure is recommended to correctly address the ill-posed problems often occurring in multi-variate optimisation. The algorithms have been successfully implemented in the PULsE software, with the latest version being immediately available for use.

Declaration of competing interest

The authors declare that they have no known competing financial interests or personal relationships that could have appeared to influence the work reported in this paper.

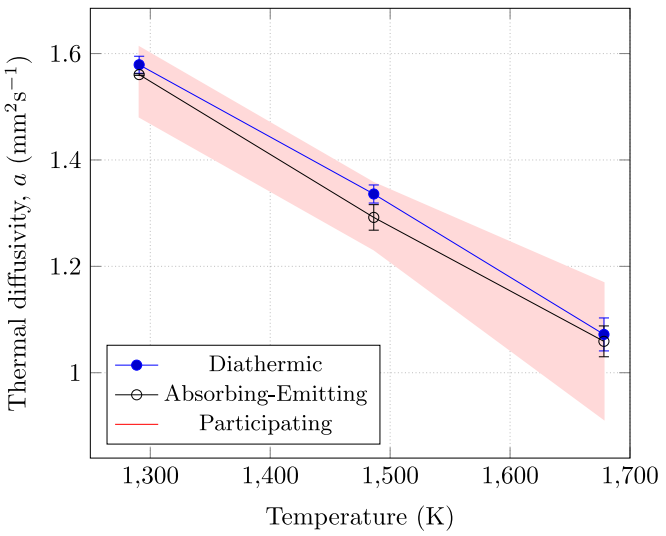

Fig. 11. Thermal diffusivity of synthetic alumina determined from a single set of experimental data using three different models. Note the uncertainties associated with the multi-variate search for the more complex problem.

Acknowledgements

This work was partially funded by the RCUK Energy Programme (Grant No. EP/T012250/1). A. L. gratefully acknowledges the experimental dataset kindly provided by Dr. A. Tenishev (MEPhI) and the involvement of Ms. A. Elbakyan in literature review.

Appendix A. Justification of using linearised boundary conditions

For the sake of simplicity, the analysis is based on the same heat conduction problem as previously described in [3]. An example distribution of the time–temperature profiles across the spatial domain is shown in Fig. A.12. Clearly, the dimensionless temperature θ can reach quite high values close to the front boundary ($y = 0$), thus indicating a possible source of error in the conventional analysis, which assumes small heating ($T - T_0 \ll T_0$). The goal is to quantify that error.

Omitting the heat equation and the initial condition, which are exactly the same as in Section 2, the problem at hand is reduced to the following set of equations:

$$\left.\frac{\partial T}{\partial z}\right|_{z=0} = -\frac{4Q}{\pi\lambda d^2}P(t) + \frac{\varepsilon(T_0)\sigma_0 T_0^4}{\lambda}\left\{\left[\frac{T_{z=0}-T_0}{T_0}+1\right]^4 - 1\right\}, \tag{A.1a}$$

$$\left.\frac{\partial T}{\partial z}\right|_{z=l} = -\frac{\varepsilon(T_0)\sigma_0 T_0^4}{\lambda}\left\{\left[\frac{T_{z=l}-T_0}{T_0}+1\right]^4 - 1\right\}, \tag{A.1b}$$

where Q is the heat absorbed by the thin surface layer and ε is the sample's flat surface emissivity. These equations are then transformed to the dimensionless form:

$$\left.\frac{\partial\theta}{\partial y}\right|_{y=0} = -\Phi(\mathrm{Fo}) + \mathrm{Bi}\cdot T_0\left[\left(\theta_{y=0}\delta T_\mathrm{m}/T_0+1\right)^4 - 1\right]/(4\delta T_\mathrm{m}), \tag{A.2a}$$

$$\left.\frac{\partial\theta}{\partial y}\right|_{y=1} = -\mathrm{Bi}\cdot T_0\left[\left(\theta_{y=1}\delta T_\mathrm{m}/T_0+1\right)^4 - 1\right]/(4\delta T_\mathrm{m}), \tag{A.2b}$$

where $\delta T_\mathrm{m} = 4Q(\pi d^2 C_\mathrm{p}\rho l)^{-1}$ is the maximum heating of the rear surface in the absence of heat sinks and $\mathrm{Bi} := 4\sigma_0\varepsilon T_0^3 l/\lambda$ is the Biot number, and $\theta = (T - T_0)/\delta T_\mathrm{m}$.

It can be easily seen that if $\theta\delta T_\mathrm{m}/T_0$ is small, the heat loss term becomes simply $\mathrm{Bi}\cdot\theta_y$, which corresponds to the classical case. When $\delta T_\mathrm{m}/T_0 \simeq 1$, using only the first term of the Taylor expansion might not be appropriate; especially at the front surface ($y = 0$, see Fig. A.12), since $\theta_{y=0} \gg \theta_{y=1}$ at $\mathrm{Fo} = 0 - 0.15$. However, the overall magnitude of the heat sink term is proportional to $T_0/4\delta T_m$. Hence, the significance of this term may be low when the expression in the brackets may be nonlinear.

The finite-difference calculations proceed as follows. The domain is divided into a uniform grid by introducing the coordinate step size $h = 1/(N-1)$, where N is the number of individual coordinate points on the grid, and the discrete time step $\tau = \tau_\mathrm{F}h^2$, $\tau_\mathrm{F} \in \mathbb{R}$. The grid is used to discretise $\theta(y, \mathrm{Fo})$, which becomes $\theta(\xi_j, \widehat{\mathrm{Fo}}_m) = \theta_j^m$, $j = 0, \ldots, N-1$, $m = 0, \ldots, m_0$, called the grid function. Let $L\phi(\xi_\alpha) = \left(\phi_{\alpha+1} - \phi_{\alpha-1}\right)/2h$. Then, the finite-difference analog of Eqs. (A.2) is:

$$L\theta_0 = -\Xi + \zeta(\theta_0), \tag{A.3a}$$

$$L\theta_{N-1} = -\zeta(\theta_{N-1}), \tag{A.3b}$$

$$\zeta(\theta_j) = \mathrm{Bi}\cdot T_0/(4\delta T_\mathrm{m})\cdot\left[(\theta_j\cdot\delta T_\mathrm{m}/T_0+1)^4 - 1\right], \tag{A.3c}$$

where the time index is implicit.

Consider using a Taylor expansion on the grid at $j = 0$ and $j = N-1$ and introducing virtual nodes $j = -1$ and $j = N$, thus transforming Eq. (A.3) using contraction mapping: $\phi = \zeta(\phi)$. For a fully-implicit scheme the first coefficients α_1 and β_1 from the tridiagonal matrix equation $\theta_j = \alpha_{j+1} + \theta_{j+1}\beta_{j+1}$ and the solution at the $j = N$ boundary are calculated at each iteration $k+1$ until the scheme converges to a given precision (usually within a few iterations):

$$[\alpha_1]^{k+1} = \frac{2\tau}{2\tau+h^2}, \tag{A.4a}$$

$$[\beta_1]^{k+1} = \frac{h^2}{2\tau+h^2}\widehat{\theta}_0 + \frac{2\tau h}{2\tau+h^2}\left[\Xi - \zeta(\theta_0^k)\right], \tag{A.4b}$$

$$[\theta_{N-1}]^{k+1} = \frac{2\tau\,[\beta_{N-1}]^k + h^2\widehat{\theta}_{N-1} - 2\tau h\zeta(\theta_{N-1}^k)}{2\tau + h^2 - 2\tau\,[\alpha_{N-1}]^k}, \tag{A.4c}$$

The solution is shown in Fig. A.13 where the heating curves have been normalised. Curves are plotted at different values of $\iota := \delta T_\mathrm{max}/T_0$, all else being equal. With increasing the ι factor, the normalised maximum shifts towards shorter times while the temperature decreases due to heat losses (in this case, $\mathrm{Bi} = 1.0$) becomes more pronounced. For $\delta T_\mathrm{max}/T_0 < 5\times10^{-2}$ (in most practical cases), this effect is so small that the nonlinear behaviour of the heat losses in Eq. (A.2) may be completely neglected. Therefore, some care must be taken only when conducting measurements at cryogenic temperatures and at a high laser power applied to poor thermal conductors. Otherwise, keeping nonlinear terms in the boundary conditions is redundant and a simpler (linearised) model of the heat problem may be used instead.

Appendix B. Numerical evaluation of some integrals

The integrand function $E_1(t)$ is discontinuous at $t = 0$, which complicates the evaluation of radiative flux derivatives $dq/d\tau$ using the standard Newton–Cotes formulae. The latter require significant computational resources, which is inappropriate when the flux derivatives need to be calculated frequently.

The general problem consists in evaluating integrals of the form:

$$I_n = \int_a^b g(t)E_n(\alpha+\beta t)dt. \tag{B.1}$$

The exponential integrals $E_n(t)$ are pre-calculated using the midpoint rule with a very large number of integration points by filling a look-up table of typically $N_\mathrm{tab} = 10{,}000$–$20{,}000$ entries, depending on the cutoff value ($t_c^\mathrm{exp} = 9.2$–21.0), which ensures a precision of at least 10^{-5}. This table is filled only once at the program start and used later in future calls to the solver. An acceptable accuracy when using a Newton–Cotes formula (e.g. the Simpson's rule) can be achieved at $n_q = 256$ [see Table B.5] for integrals of order $n \geq 2$ when the integrand is well-defined at zero. Since the exponential integrals rapidly decrease with τ and the emission function $j(t)$ is bounded, the integrand becomes very small where the exponential integrals are near-zero. The integration bounds are calculated as $[\max\{a, (t_c - \alpha)/\beta\}, b]$

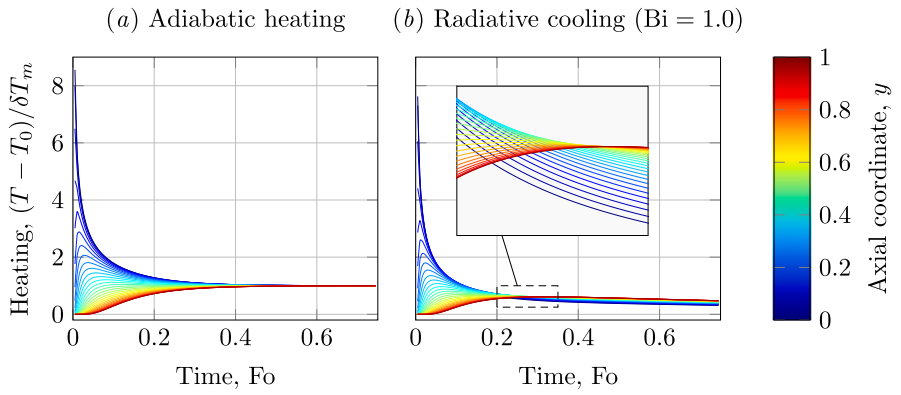

Fig. A.12. Full time–temperature profile as calculated from the linearised one-dimensional problem after a $\mathrm{Fo_{las}} = 1 \times 10^{-4}$ pulse (fully implicit scheme, $N = 30$). Note the crossover of thermograms at different y for the radiative cooling.

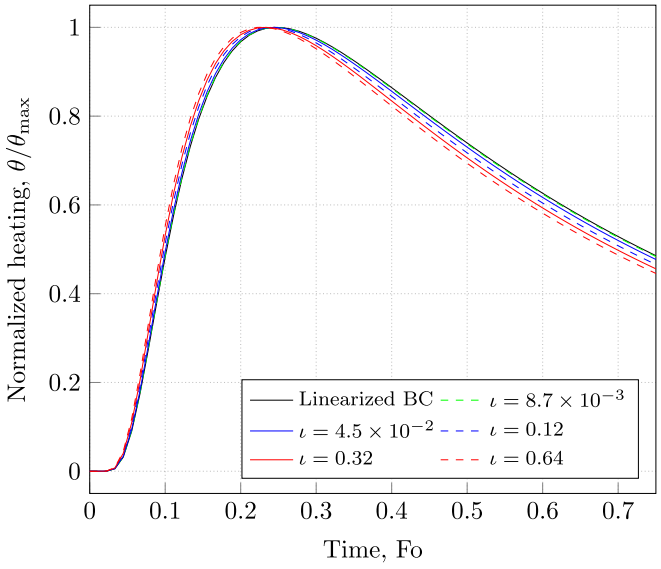

Fig. A.13. The effect of nonlinear heat losses (Eqs. (A.2)) on the shape of the rear-surface heating curve evaluated by solving the boundary problem at different values of $\iota = \delta T_m/T_0$ using a fully-implicit finite-difference scheme and a fixed-point iteration algorithm (Bi = 1.0, $\mathrm{Fo_{las}} \approx 5 \times 10^{-3}$, fixed-point error tolerance $\Delta_1 = 10^{-8}$ K).

at $\beta < 0$ and $[a, \min\{b, (t_c - \alpha)/\beta\}]$ at $\beta > 0$. This ensures that for large τ_0, the integration excludes terms smaller in amplitude than a certain threshold defined by the cutoff t_c. Additionally, since $f(t)$ is discretised differently to what is used in the quadrature scheme, a natural cubic spline interpolation implemented in The Apache Commons Mathematics Library is introduced to calculate the function values.

A more effective quadrature has been introduced by Chandrasekhar [20]. It is first noticed that Eq. (B.1) may be written as:

$$\int_{\alpha+\beta a}^{\alpha+\beta b} g\left(\beta(x-\alpha)\right) E_n(x)dx = \sum_{j=1}^{m} a_j g(x_j). \tag{B.2}$$

The moments M_l are defined as:

$$M_l = \int_{\alpha+\beta a}^{\alpha+\beta b} x^l E_n(x)dx. \tag{B.3}$$

These can be integrated by parts if the recurrent expression for $E_n(x)$ is utilised [20]. After the moments have been calculated, the next step is to calculate the x_j $(j = 1, \ldots, m)$ roots of the monic polynomial $x^m + \sum_{l=0}^{m-1} c_l x^l$ where the coefficients c_l form the solution of a linear

Table B.5
Comparison between quadrature formulae for calculating $I_2 = \int_0^{\tau_0} j[\theta(t)]E_2(\alpha + \beta t)dt$ at $\tau_0 = 2.0$, $\beta = -1$, $\alpha = \tau_0$ using a test temperature profile.

Simpson's rule			Chandrasekhar's quadrature		
n	I_2	Δ	m	I_2	Δ
32	940.70148	–	2	940.10042	–
256	940.10960	−0.59190	4	940.09943	−0.00112
4096	940.10074	−0.00886	8	940.09948	+0.00005

Table B.6
Comparison of end precision Δ and computational effort $T_{10,000}$ (measured for 10,000 consecutive calls to the respective integration method) for different quadrature formulae for calculating the integral $I_1 = \int_\tau^{\tau_0} j[\theta(t)]E_1(\alpha + \beta t)dt$ at $\tau_0 = 3.0$, $\beta = 1$, $\tau = -\alpha = 0.5$ using the same test temperature profile as in Table B.5.

Simpson's rule				Chandrasekhar's quadrature			
n	I_1	Δ	$T_{10,000}$ (ms)	m	I_1	Δ	$T_{10,000}$ (ms)
32	2190.51	–	20	2	1961.618	–	82
256	1976.71	−213.8	121	3	1961.617	−0.001	163
4096	1962.31	−14.4	1254	8	1961.617	0	620

set:

$$M_{i+m} + \sum_{l=0}^{m-1} c_l M_{i+l} = 0, \quad i = 0, 1, \ldots, m-1. \tag{B.4}$$

In fact, the latter is effectively a matrix equation, which may simply be solved using matrix inversion. The roots x_j are then found with the help of a Laguerre solver implemented in the Apache Commons Mathematics Library. The weights a_j of the quadrature Eq. (B.2) should satisfy the m equations:

$$M_l = \sum_{j=1}^{m} a_j x_j^l, \quad l = 0, \ldots, m-1. \tag{B.5}$$

This is solved in a similar fashion. Tables B.5 and B.6 show test results of using the Chandrasekhar's quadrature versus the Newton–Cotes formulae. These test have been carried out for a test temperature profile shown in Fig. 4.

References

[1] T. Pavlov, M. Wenman, L. Vlahovic, D. Robba, R. Konings, P. Van Uffelen, R. Grimes, Measurement and interpretation of the thermo-physical properties of UO_2 at high temperatures: The viral effect of oxygen defects, Acta Mater. 139 (2017) 138–154, http://dx.doi.org/10.1016/j.actamat.2017.07.060.

[2] S. Zhao, X. Sun, Z. Li, W. Xie, S. Meng, C. Wang, W. Zhang, Simultaneous retrieval of high temperature thermal conductivities, anisotropic radiative properties, and thermal contact resistance for ceramic foams, Appl. Therm. Eng. 146 (2019) 569–576, http://dx.doi.org/10.1016/j.applthermaleng.2018.10.021.

[3] A. Lunev, R. Heymer, Decreasing the uncertainty of classical laser flash analysis using numerical algorithms robust to noise and systematic errors, Rev. Sci. Instrum. 91 (6) (2020) 064902, http://dx.doi.org/10.1063/1.5132786.

[4] M. Lazard, S. André, D. Maillet, Diffusivity measurement of semi-transparent media: model of the coupled transient heat transfer and experiments on glass, silica glass and zinc selenide, Int. J. Heat Mass Transfer 47 (3) (2004) 477–487, http://dx.doi.org/10.1016/j.ijheatmasstransfer.2003.07.003.

[5] T. Olorunyolemi, A. Birnboim, Y. Carmel, O.C. Wilson Jr., I.K. Lloyd, S. Smith, R. Campbell, Thermal conductivity of zinc oxide: From green to sintered state, J. Am. Ceram. Soc. 85 (5) (2002) 1249–1253, http://dx.doi.org/10.1111/j.1151-2916.2002.tb00253.x.

[6] K. Itatani, T. Tsujimoto, A. Kishimoto, Thermal and optical properties of transparent magnesium oxide ceramics fabricated by post hot-isostatic pressing, J. Eur. Ceram. Soc. 26 (4) (2006) 639–645, http://dx.doi.org/10.1016/j.jeurceramsoc.2005.06.011, Proceedings of the International Symposium on Inorganic and Environmental Materials, Eindhoven, NL, October 2004.

[7] C. Cozzo, D. Staicu, J. Somers, A. Fernandez, R. Konings, Thermal diffusivity and conductivity of thorium–plutonium mixed oxides, J. Nucl. Mater. 416 (1) (2011) 135–141, http://dx.doi.org/10.1016/j.jnucmat.2011.01.109, Nuclear Materials IV.

[8] P. Bison, F. Cernuschi, E. Grinzato, S. Marinetti, D. Robba, Ageing evaluation of thermal barrier coatings by thermal diffusivity, Infrared Phys. Technol. 49 (3) (2007) 286–291, http://dx.doi.org/10.1016/j.infrared.2006.06.019.

[9] M. Tischler, J.J. Kohanoff, G.A. Rangugni, G. Ondracek, Pulse method of measuring thermal diffusivity and optical absorption depth for partially transparent materials, J. Appl. Phys. 63 (5) (1988) 1259–1264, http://dx.doi.org/10.1063/1.339950.

[10] R.L. McMasters, J.V. Beck, R.B. Dinwiddie, H. Wang, Accounting for penetration of laser heating in flash thermal diffusivity experiments, J. Heat Transfer 121 (1) (1999) 15–21, http://dx.doi.org/10.1115/1.2825929.

[11] J. Blumm, J.B. Henderson, O. Nilsson, J. Fricke, Laser flash measurement of the phononic thermal diffusivity of glasses in the presence of ballistic radiative transfer, High Temp.. High Press. (Print) 29 (5) (1997) 555–560.

[12] H. Mehling, G. Hautzinger, O. Nilsson, J. Fricke, R. Hofmann, O. Hahn, Thermal diffusivity of semitransparent materials determined by the laser-flash method applying a new analytical model, Int. J. Thermophys. 19 (3) (1998) 941–949.

[13] S. Andre, A. Degiovanni, A theoretical study of the transient coupled conduction and radiation heat transfer in glass: phonic diffusivity measurements by the flash technique, Int. J. Heat Mass Transfer 38 (18) (1995) 3401–3412, http://dx.doi.org/10.1016/0017-9310(95)00075-K.

[14] S. Andre, A. Degiovanni, A new way of solving transient radiative-conductive heat transfer problems, J. Heat Transfer 120 (4) (1998) 943–955, http://dx.doi.org/10.1115/1.2825914.

[15] M. Lazard, S. Andre, D. Maillet, D. Baillis, A. Degiovanni, Flash experiment on a semitransparent material: interest of a reduced model, Inverse Probl. Eng. 9 (4) (2001) 413–429, http://dx.doi.org/10.1080/174159701088027772.

[16] M. Lazard, S. André, D. Maillet, Transient coupled radiative–conductive heat transfer in a gray planar medium with anisotropic scattering, J. Quant. Spectrosc. Radiat. Transfer 69 (1) (2001) 23–33, http://dx.doi.org/10.1016/S0022-4073(00)00054-6.

[17] A. Braiek, A. Adili, F. Albouchi, M. Karkri, S.B. Nasrallah, Estimation of radiative and conductive properties of a semitransparent medium using genetic algorithms, Meas. Sci. Technol. 27 (6) (2016) 065601, http://dx.doi.org/10.1088/0957-0233/27/6/065601.

[18] M.F. Modest, F.H. Azad, The influence and treatment of mie-anisotropic scattering in radiative heat transfer, J. Heat Transfer 102 (1) (1980) 92–98, http://dx.doi.org/10.1115/1.3244255.

[19] O. Hahn, F. Raether, M. Arduini-Schuster, J. Fricke, Transient coupled conductive/radiative heat transfer in absorbing, emitting and scattering media: application to laser-flash measurements on ceramic materials, Int. J. Heat Mass Transfer 40 (3) (1997) 689–698, http://dx.doi.org/10.1016/0017-9310(96)00137-8.

[20] S. Chandrasekhar, Radiative Transfer, Dover Publications (New York, NY), 1960.

[21] Z. da Silva, M. Laurent, D. Baillis-Doermann, Inverse analysis of transient coupled conduction-radiation-conductive and radiative properties and measurements, in: 7th AIAA/ASME Joint Thermophysics and Heat Transfer Conference, 1998, p. 2842.

[22] R. Coquard, D. Rochais, D. Baillis, Experimental investigations of the coupled conductive and radiative heat transfer in metallic/ceramic foams, Int. J. Heat Mass Transfer 52 (21) (2009) 4907–4918, http://dx.doi.org/10.1016/j.ijheatmasstransfer.2009.05.015.

[23] R. Coquard, J. Randrianalisoa, S. Lallich, D. Baillis, Extension of the FLASH method to semitransparent polymer foams, J. Heat Transfer 133 (11) (2011) http://dx.doi.org/10.1115/1.4004392.

[24] O. Wellele, H. Orlande, N. Ruperti, M. Colaço, A. Delmas, Coupled conduction–radiation in semi-transparent materials at high temperatures, J. Phys. Chem. Solids 67 (9) (2006) 2230–2240, http://dx.doi.org/10.1016/j.jpcs.2006.06.007, SMEC 2005.

[25] J. Zmywaczyk, P. Koniorczyk, Numerical solution of inverse radiative–conductive transient heat transfer problem in a grey participating medium, Int. J. Thermophys. 30 (4) (2009) 1438–1451.

[26] D. Lacroix, G. Parent, F. Asllanaj, G. Jeandel, Coupled radiative and conductive heat transfer in a non-grey absorbing and emitting semitransparent media under collimated radiation, J. Quant. Spectrosc. Radiat. Transfer 75 (5) (2002) 589–609, http://dx.doi.org/10.1016/S0022-4073(02)00031-6.

[27] M. Sans, V. Schick, G. Parent, O. Farges, Experimental characterization of the coupled conductive and radiative heat transfer in ceramic foams with a flash method at high temperature, Int. J. Heat Mass Transfer 148 (2020) 119077, http://dx.doi.org/10.1016/j.ijheatmasstransfer.2019.119077.

[28] W.A. Fiveland, Discrete-ordinates solutions of the radiative transport equation for rectangular enclosures, J. Heat Transfer 106 (4) (1984) 699–706, http://dx.doi.org/10.1115/1.3246741.

[29] W.A. Fiveland, Discrete ordinate methods for radiative heat transfer in isotropically and anisotropically scattering media, J. Heat Transfer 109 (3) (1987) 809–812, http://dx.doi.org/10.1115/1.3248167.

[30] K.D. Lathrop, B.G. Carlson, Discrete Ordinates Angular Quadrature of the Neutron Transport Equation, Technical Report, Los Alamos Scientific Lab., N. Mex., 1964.

[31] P. Coelho, A comparison of spatial discretization schemes for differential solution methods of the radiative transfer equation, J. Quant. Spectrosc. Radiat. Transfer 109 (2) (2008) 189–200, http://dx.doi.org/10.1016/j.jqsrt.2007.08.012, The Fifth International Symposium on Radiative Transfer.

[32] P.J. Coelho, Advances in the discrete ordinates and finite volume methods for the solution of radiative heat transfer problems in participating media, J. Quant. Spectrosc. Radiat. Transfer 145 (2014) 121–146, http://dx.doi.org/10.1016/j.jqsrt.2014.04.021.

[33] A. Philipp, J.F. Eichinger, R.C. Aydin, A. Georgiadis, C.J. Cyron, M. Retsch, The accuracy of laser flash analysis explored by finite element method and numerical fitting, Heat Mass Transf. 56 (3) (2020) 811–823.

[34] A. Lunev, Kotik-coder/PULsE: PULsE v1.79, 2020, http://dx.doi.org/10.5281/zenodo.3928762.

[35] E.J. Yoffa, Role of carrier diffusion in lattice heating during pulsed laser annealing, Appl. Phys. Lett. 36 (1) (1980) 37–38, http://dx.doi.org/10.1063/1.91306.

[36] M. Brunner, M.-A. Thermitus, Method and device for the photothermic investigation of a sample, 2019, US Patent 10, 180, 358.

[37] J.R. Howell, M.P. Menguc, R. Siegel, Thermal Radiation Heat Transfer, CRC press, 2010.

[38] J.W. Demmel, Applied Numerical Linear Algebra, Vol. 56, Siam, 1997.

[39] A.A. Samarskii, The Theory of Difference Schemes, Vol. 240, CRC Press, 2001.

[40] V. Kourganoff, Basic Methods in Transfer Problems, Dover, 1963.

[41] M.F. Modest, Radiative Heat Transfer, Academic press, 2013.

[42] R. Cess, The interaction of thermal radiation with conduction and convection heat transfer, in: T.F. Irvine, J.P. Hartnett (Eds.), Advances in Heat Transfer, Vol. 1, Elsevier, 1964, pp. 1–50, http://dx.doi.org/10.1016/S0065-2717(08)70096-0.

[43] A. Schuster, Radiation through a foggy atmosphere, Astrophys. J. 21 (1905) 1.

[44] K. Schwartzschild, W. Gesell, Gottingen, nachr. math, Phys. Klasse (1906) 41.

[45] M. Brewster, C. Tien, Examination of the two-flux model for radiative transfer in particular systems, Int. J. Heat Mass Transfer 25 (12) (1982) 1905–1907, http://dx.doi.org/10.1016/0017-9310(82)90113-2.

[46] M. Mengüç, R. Viskanta, Comparison of radiative transfer approximations for a highly forward scattering planar medium, J. Quant. Spectrosc. Radiat. Transfer 29 (5) (1983) 381–394, http://dx.doi.org/10.1016/0022-4073(83)90111-5.

[47] H. Engler, Computation of scattering kernels in radiative transfer, J. Quant. Spectrosc. Radiat. Transfer 165 (2015) 38–42, http://dx.doi.org/10.1016/j.jqsrt.2015.06.019.

[48] H.C. van de Hulst, Light Scattering by Small Particles, Courier Corporation, 1981.

[49] L.G. Henyey, J.L. Greenstein, Diffuse radiation in the galaxy, Astrophys. J. 93 (1941) 70–83.

[50] G.W. Kattawar, A three-parameter analytic phase function for multiple scattering calculations, J. Quant. Spectrosc. Radiat. Transfer 15 (9) (1975) 839–849.

[51] V.I. Haltrin, One-parameter two-term henyey-greenstein phase function for light scattering in seawater, Appl. Opt. 41 (6) (2002) 1022–1028.

[52] J. Wang, C. Xu, A.M. Nilsson, D.L.A. Fernandes, G.A. Niklasson, A novel phase function describing light scattering of layers containing colloidal nanospheres, Nanoscale 11 (2019) 7404–7413, http://dx.doi.org/10.1039/C9NR01707K.

[53] S. Zhao, X. Sun, Q. Que, W. Zhang, Influence of scattering phase function on estimated thermal properties of Al_2O_3 ceramic foams, Int. J. Thermophys. 40 (1) (2019) 11.

[54] P. Boulet, A. Collin, J. Consalvi, On the finite volume method and the discrete ordinates method regarding radiative heat transfer in acute forward anisotropic scattering media, J. Quant. Spectrosc. Radiat. Transfer 104 (3) (2007) 460–473, http://dx.doi.org/10.1016/j.jqsrt.2006.09.010.

[55] J.P. Jessee, W.A. Fiveland, Bounded, high-resolution differencing schemes applied to the discrete ordinates method, J. Thermophys. Heat Transfer 11 (4) (1997) 540–548, http://dx.doi.org/10.2514/2.6296.

[56] E. Hairer, G. Wanner, Solving Ordinary Differential Equations II. Stiff and Differential-Algebraic Problems, Vol. 14, 1996, http://dx.doi.org/10.1007/978-3-662-09947-6.

[57] F. Liu, H.A. Becker, A. Pollard, Spatial differencing schemes of the discrete-ordinates method, Numer. Heat Transfer B 30 (1) (1996) 23–43, http://dx.doi.org/10.1080/10407799608915070.

[58] P.G. Maginot, J.C. Ragusa, J.E. Morel, High-order solution methods for grey discrete ordinates thermal radiative transfer, J. Comput. Phys. 327 (2016) 719–746, http://dx.doi.org/10.1016/j.jcp.2016.09.055.
[59] R. Alexander, Diagonally implicit runge–kutta methods for stiff O.D.E.'s, SIAM J. Numer. Anal. 14 (6) (1977) 1006–1021, http://dx.doi.org/10.1137/0714068.
[60] V. D'Alessandro, L. Binci, S. Montelpare, R. Ricci, On the development of openfoam solvers based on explicit and implicit high-order runge–kutta schemes for incompressible flows with heat transfer, Comput. Phys. Comm. 222 (2018) 14–30, http://dx.doi.org/10.1016/j.cpc.2017.09.009.
[61] P.D. Boom, D.W. Zingg, Optimization of high-order diagonally-implicit runge–kutta methods, J. Comput. Phys. 371 (2018) 168–191, http://dx.doi.org/10.1016/j.jcp.2018.05.020.
[62] C.A. Kennedy, M.H. Carpenter, Diagonally implicit Runge-Kutta methods for ordinary differential equations. A review, Techical Report, NASA Langley Research Center, Hampton, VA, United States, 2016.
[63] D.S. Blom, P. Birken, H. Bijl, F. Kessels, A. Meister, A.H. van Zuijlen, A comparison of rosenbrock and ESDIRK methods combined with iterative solvers for unsteady compressible flows, Adv. Comput. Math. 42 (6) (2016) 1401–1426.
[64] J. Dormand, P. Prince, A family of embedded runge-kutta formulae, J. Comput. Appl. Math. 6 (1) (1980) 19–26, http://dx.doi.org/10.1016/0771-050X(80)90013-3.
[65] P. Bogacki, L.F. Shampine, A 3 (2) pair of runge-kutta formulas, Appl. Math. Lett. 2 (4) (1989) 321–325.
[66] E. Hairer, S.P. Nørsett, G. Wanner, Solving Ordinary Differential Equations I. Nonstiff Problems, Springer Series in Computational Mathematics, 1993.
[67] M. Hosea, L. Shampine, Analysis and implementation of TR-BDF2, Appl. Numer. Math. 20 (1) (1996) 21–37, http://dx.doi.org/10.1016/0168-9274(95)00115-8, Method of Lines for Time-Dependent Problems.
[68] L.C. Nitsche, One-dimensional stretching functions for cn patched grids, and associated truncation errors in finite-difference calculations, Commun. Numer. Methods. Eng. 12 (5) (1996) 303–316, http://dx.doi.org/10.1002/(SICI)1099-0887(199605)12:5<303::AID-CNM979>3.0.CO;2-C.
[69] M. Vinokur, On one-dimensional stretching functions for finite-difference calculations, J. Comput. Phys. 50 (2) (1983) 215–234, http://dx.doi.org/10.1016/0021-9991(83)90065-7.
[70] D.F. Rogers, J.A. Adams, Mathematical Elements for Computer Gaphics, McGraw-Hill Higher Education, 1989.
[71] J.S. Truelove, Discrete-ordinate solutions of the radiation transport equation, J. Heat Transfer 109 (4) (1987) 1048–1051, http://dx.doi.org/10.1115/1.3248182.
[72] S. Kumar, A. Majumdar, C.L. Tien, The differential-discrete-ordinate method for solutions of the equation of radiative transfer, J. Heat Transfer 112 (2) (1990) 424–429, http://dx.doi.org/10.1115/1.2910395.
[73] B.-W. Li, Q. Yao, X.-Y. Cao, K.-F. Cen, A new discrete ordinates quadrature scheme for three-dimensional radiative heat transfer, J. Heat Transfer 120 (2) (1998) 514–518, http://dx.doi.org/10.1115/1.2824279.
[74] L. Liu, L. Ruan, H. Tan, On the discrete ordinates method for radiative heat transfer in anisotropically scattering media, Int. J. Heat Mass Transfer 45 (15) (2002) 3259–3262, http://dx.doi.org/10.1016/S0017-9310(02)00035-2.
[75] R. Koch, R. Becker, Evaluation of quadrature schemes for the discrete ordinates method, J. Quant. Spectrosc. Radiat. Transfer 84 (4) (2004) 423–435, http://dx.doi.org/10.1016/S0022-4073(03)00260-7, Eurotherm Seminar 73 - Computational Thermal Radiation in Participating Media.
[76] V. Lebedev, Quadratures on a sphere, USSR Comput. Math. Math. Phys. 16 (2) (1976) 10–24, http://dx.doi.org/10.1016/0041-5553(76)90100-2.
[77] S.T. Thynell, Discrete-ordinates method in radiative heat transfer, Internat. J. Engrg. Sci. 36 (12) (1998) 1651–1675, http://dx.doi.org/10.1016/S0020-7225(98)00052-4.
[78] L.A. Dombrovsky, J.H. Randrianalisoa, W. Lipiski, D. Baillis, Approximate analytical solution to normal emittance of semi-transparent layer of an absorbing, scattering, and refracting medium, J. Quant. Spectrosc. Radiat. Transfer 112 (12) (2011) 1987–1994, http://dx.doi.org/10.1016/j.jqsrt.2011.04.008.
[79] A.N. Tikhonov, On the solution of ill-posed problems and the method of regularization, Dokl. Akad. Nauk 151 (3) (1963) 501–504.
[80] P.E. Gill, W. Murray, M.H. Wright, Practical Optimization, SIAM, 2019.
[81] V. Baranov, A. Tenishev, A. Lunev, S. Pokrovskii, A. Khlunov, High-temperature measurements of the thermal conductivity of reactor materials by the laser flash method, Yad. Fiz. Inzhin 2 (4) (2011) 291–302.
[82] D. Ditmars, S. Ishihara, S. Chang, G. Bernstein, E. West, Enthalpy and heat-capacity standard reference material: synthetic sapphire (α-Al_2O_3) from 10 to 2250 k, J. Res. Natl. Bur. Stand. 87 (2) (1982) 159–163.
[83] C.J. Engberg, E.H. Zaehms, Thermal expansion of Al_2O_3, BeO, MgO, B_4C, SiC, and TiC above 1000C, J. Am. Ceram. Soc. 42 (6) (1959) 300–305, http://dx.doi.org/10.1111/j.1151-2916.1959.tb12958.x.